Rate equations, spatial moments, and concentration profiles for mobile-immobile models with power-law and mixed waiting time distributions

Timo J. Doerries,[1] Aleksei V. Chechkin,[1,2,3] Rina Schumer,[4] and Ralf Metzler[1,*]

[1]*Institute of Physics and Astronomy, University of Potsdam, 14476 Potsdam, Germany*

[2]*Faculty of Pure and Applied Mathematica, Hugo Steinhaus Center, Wrocław University of Science and Technology, Wyspianskiego 27, 50-370 Wrocław, Poland*

[3]*Akhiezer Institute for Theoretical Physics, 61108 Kharkov, Ukraine*

[4]*Desert Research Institute, Reno, Nevada 89512, USA*

(Received 1 October 2021; accepted 17 December 2021; published 4 January 2022)

We present a framework for systems in which diffusion-advection transport of a tracer substance in a mobile zone is interrupted by trapping in an immobile zone. Our model unifies different model approaches based on distributed-order diffusion equations, exciton diffusion rate models, and random-walk models for multirate mobile-immobile mass transport. We study various forms for the trapping time dynamics and their effects on the tracer mass in the mobile zone. Moreover, we find the associated breakthrough curves, the tracer density at a fixed point in space as a function of time, and the mobile and immobile concentration profiles and the respective moments of the transport. Specifically, we derive explicit forms for the anomalous transport dynamics and an asymptotic power-law decay of the mobile mass for a Mittag-Leffler trapping time distribution. In our analysis we point out that even for exponential trapping time densities, transient anomalous transport is observed. Our results have direct applications in geophysical contexts, but also in biological, soft matter, and solid state systems.

DOI: 10.1103/PhysRevE.105.014105

I. INTRODUCTION

In their original formulations of Brownian motion, Einstein [1], von Smoluchowski [2], Sutherland [3], and Langevin [4] assumed an isotropic homogeneous environment, and thus a constant diffusion coefficient D. In the hydrodynamic limit, these theories led to the standard diffusion equation (Fick's second law [5]) for the probability density function (PDF) $P(\mathbf{r},t)$ to find the Brownian particle at position $\mathbf{r}$ at time t [6,7]. In more mathematical terms this means that increments of Brownian motion, on a coarse-grained level [8], are independent and identically distributed random variables [9]. Apart from the linear time dependence $\langle \mathbf{r}^2(t)\rangle \propto Dt$ of the mean-square displacement (MSD), the quintessential consequence of these assumptions is the Gaussian PDF of a Brownian particle, $P(\mathbf{r},t) = (4\pi Dt)^{-d/2}\exp(-\mathbf{r}^2/4Dt)$ in d spatial dimensions [7,9]. However, already in 1926 Richardson concluded from measurements of the stochastic motion of two pilot balloons in a turbulent atmosphere that the relative spreading, i.e., the diffusion coefficient for the relative coordinate of the balloons, increases with their distance l, and he fitted the data with the function $D(l) = \varepsilon l^{4/3}$ with the constant $\varepsilon \approx 0.4\ \mathrm{cm}^{2/3}/\mathrm{sec}$. [10]. Batchelor, in his work on homogeneous turbulence, showed that the second moment of the Richardson process can also be obtained by using the time-dependent scaling $D(t) \propto t^2$ of the diffusivity instead of the Richardson 4/3 law [11]. Today, anomalous diffusion with a power-law form $\langle \mathbf{r}^2(t)\rangle \propto t^\alpha$ is known from a wide range of systems. Based on the value of the anomalous diffusion exponent, one typically distinguished subdiffusion for $0 < \alpha < 1$ and superdiffusion for $\alpha > 1$ [12–18].

The MSD and the particle displacement PDF are highly relevant quantities and they can be measured relatively straightforwardly in modern single-particle-tracking experiments [17,19]. However, they require relatively extensive experimental setups on geological scales [20]. In a typical geophysical field experiment, as schematically depicted in Fig. 1(a), a solute or a fine particle substance is injected into the site and its concentration is measured at selected points in space as a function of time [20–24]. For Brownian tracer particles advected with a drift velocity $\mathbf{v}$, the concentration profile has the shape $C(\mathbf{r},t) \simeq (Dt)^{-d/2}\exp(-[\mathbf{r}-\mathbf{v}t]^2/4Dt)$. In many geophysical experiments the value of the PDF is measured at a given point $\mathbf{r}_0$ in space, as a function of time. This so-called breakthrough curve (BTC) at long times then shows an asymptotic exponential decay of the tracer concentration.

In contrast to this Brownian picture, power-law tails in the time dependence of BTCs have consistently been reported from the centimeter scale in the laboratory to field experiments on kilometer scales [22,25]. One example for such an experiment was reported in [22] based on the injection of fluorescent dye into sinking surface water leading to a karst aquifer under the Schwarzwasser valley, where BTCs were measured up to 7400 m away from the injection point. In such settings, the tracer motion is interrupted by immobilization periods, e.g., in dead-end pores with negligible flow, in which tracers are effectively trapped [24,26,27].

The continuous-time random walk (CTRW) is a well-established model describing power-law-tailed BTCs [22,28–32]. In a CTRW a single tracer jumps instantaneously,

*rmetzler@uni-potsdam.de

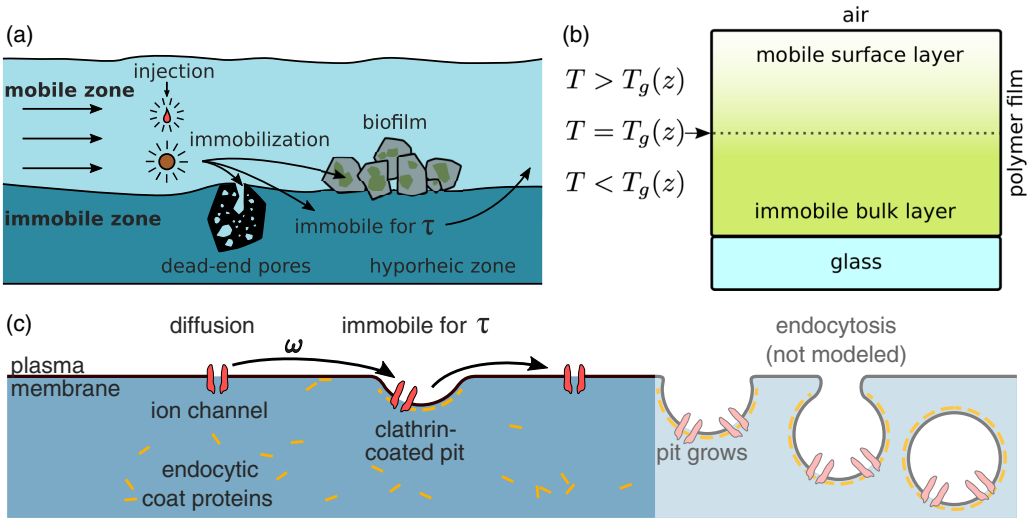

FIG. 1. Examples for systems with MIM zones. (a) Schematic of a tracer test in a typical geophysical setting. Dye or fine particles are injected into the mobile zone of a groundwater system or river. In our extended mobile-immobile model, which is based on [65,66], the tracers immobilize in dead-end pores, the hyporheic zone, or biofilms for a random time τ drawn from a probability density $\gamma(\tau)$ [see Eq. (1) for details]. After the period τ the tracers move back into the mobile zone. (b) Schematic of a thin polymer film on a glass substrate with depth-dependent glass transition temperature $T_g(z)$. Fluorescent dye is immobile in the bulk layer but mobile in the surface layer. (Figure was adapted from [59].) (c) Potassium channels diffuse in the plasma membrane of human embryonic kidney cells. Endocytic coat proteins assemble at the plasma membrane and generate clathrin-coated pits, to which the channel binds upon encounter. The majority of channels leave the pit before the clathrin-mediated endocytosis is completed. (Figure was adapted from [63].)

with variable jump lengths and waiting times drawn from respective PDFs [33,34]. A CTRW with scale-free power-law-distributed waiting times and jump lengths with a finite variance was originally introduced in the description of charge carrier motion in amorphous semiconductors [35] and is closely connected to the quenched energy landscape model [35–37]. When the waiting time PDF has a power-law tail of the form proportional to $t^{-1-\mu}$ with $0 < \mu < 1$, the associated mean waiting time diverges and anomalous non-Fickian diffusion arises [33–35]. In the quenched trap model, power-law waiting time PDFs are effected by exponential distributions of trap depths [36]. In contrast, in the model developed in [38] a particle undergoes Fickian diffusion which is interrupted by binding to spherical traps. All traps have the same binding energy. Using equilibrium statistics reveals that the densities of particles inside and outside the traps are linearly coupled with a refilling and an escape rate. This yields a linear MSD with rescaled time $t \to t/(1+\lambda)$ with a positive parameter λ depending on the mean trapping time and trap density. For biased transport, the case of $1 < \mu < 2$ with finite mean waiting time but infinite variance still exhibits transport anomalies [39]. A power-law waiting time PDF (with exponential long-time cutoff reflecting the finiteness of the system) was indeed reconstructed from the hydraulic conductivity field in a heterogeneous porous medium [31]. Retention of chlorine tracer in catchments was also connected with power-law or Γ-distributed immobilization times [40,41]. In the CTRW picture the PDF $P(\mathbf{r}, t)$ does not distinguish between mobile and trapped particles [42].

Often, experiments in a geophysical setting yield incomplete mass recovery [20,22–24]. For instance, the setup of the first macrodispersion experiment consisted of an array of multilevel samplers and flow meters to obtain the plume of bromide injected into a heterogeneous aquifer [20,43]. The total recovered mass monotonically decreased [20]. In addition, only (or preferably) tracers that are not immobilized may be measured, because they need to enter the detector, e.g., from a groundwater spring [22,26,44,45]. In such situations it is thus desirable to have a model that separates the mobile and immobile particle fractions. In order to distinguish between mobile and immobile particles within the CTRW a particle is defined to be mobile if it moves within a preset time interval [29]. It follows that for an exponential waiting time all particles are mobile for preset time intervals sufficiently longer than the characteristic waiting time [29].

A modeling approach that explicitly separates the two particle fractions and that is particularly popular in hydrology modeling is the mobile-immobile model (MIM) splitting the domain into mobile and immobile zones as depicted in Fig. 1(a) [26,45–49]. The description in MIM-type models typically considers one or two spatial dimensions, while transitions between the two zones occur along an eliminated dimension. In contrast to the CTRW model, where a single concentration profile describes all tracers, the MIM thus splits the concentration into a mobile and an immobile concentration [22,26,29,49]. Including a power-law distribution of transition rates between the zones yields power-law tailed BTCs. This model, called fractal MIM [45], is closely related to bifractional differential equations. Most notably in the context of this work, the MIM has been applied successfully to geophysical systems such as groundwater aquifers, rivers, and porous media [20–22,24,26,44,50,51]. Understanding the motion of introduced tracers in such systems is of high relevance

to understand the dynamics of contaminants in freshwater sources [21,22].

Figure 1(a) shows a schematic of such systems. In addition to dead-end pores, in another scenario the tracer can immobilize in streambed (benthic) biofilms [50,52–54]. Specifically, the attenuation of endocrine disruptors in a stream is attributed to sorption and biochemical reactions in biofilms [55]. Likely, adding wood to streams creates additional depositional areas for fine particles and bacteria, effectively increasing the immobile capacity [56]. Moreover, we mention the hyporheic zone, the region of near-stream aquifers [24] that is important for, *inter alia*, microplastic retention [57]. In addition, the hyporheic zone plays an important role in removing organic compounds from wastewater treatment plants that enter streams [58]. The reactivity of, e.g., metformin, a diabetes drug, is approximately 25 times higher in the hyporheic zone as compared to the in-stream reactivity [58]. The removal depends on hyporheic exchange fluxes [58]. The exchange of tracers between the mobile zone of a stream and the hyporheic zone has been studied intensively using MIM-type approaches [21,45,50].

Importantly, applications of MIM-type models go beyond geophysical settings. We mention that mobile and immobile zones can be found in polymer systems as shown in Fig. 1(b): A thin polymer film mounted on top of a glass support is kept at a temperature T slightly below the bulk glass transition temperature T_g [59]. Due to surface effects T_g is actually a decreasing function of the height z above the glass surface. Depending on z, the polymer is split into an immobile bulk layer and a shallow mobile surface layer [59–61]. Single-molecule-tracking experiments of fluorescent dyes in the polymer film corroborate this picture [59]. A second example is the transport of dye in crystalline microporous coordination polymers, showing a pronounced splitting into populations of fast, slow, and slowest fractions [62].

Another example with mobile and immobile zones stems from biophysics and is shown in Fig. 1(c). Here the potassium channel Kv2.1 diffuses in the plasma membrane of a human embryonic kidney cell. Upon encountering a clathrin-coated pit, the channels immobilize [63]. A small portion of the channels in the pit is transferred inside the cell via clathrin-mediated endocytosis [63]. The majority of channels escape the pit and continue to diffuse. The immobilization time statistic follows a power-law waiting time density with scaling exponent $\mu \approx 0.9$ [63].

In what follows we introduce and discuss in detail the extended mobile-immobile model (EMIM) describing the mobile and immobile concentrations of a given tracer substance. The dynamics is governed by a trapping time PDF of particles in the immobile zone, which in contrast to the MIM is not restricted to an exponential dynamic and is well defined in the short-time limit as compared to the case of a power-law-tailed PDF in the fractal MIM. We choose PDFs with and without characteristic waiting times. Note that while the EMIM we develop here is relevant to a broad range of systems, we will mainly use geophysical language in what follows. The reason is that this is the one of the most classical fields in which MIM-type models have been applied. However, the probabilistic formulation makes it easily accessible, and amenable for modifications, in other fields.

The paper is organized as follows. In Sec. II we present our EMIM in terms of partial integro-differential equations, we present general expressions such as the mobile mass and transport moments, and we present the BTCs. We obtain specific expressions for the observables in the EMIM and discuss possible extensions in Sec. III. In Sec. IV we derive from our EMIM bifractional models equivalent to the fractal MIM and obtain exact expressions for the moments using these models. A detailed comparison of the time evolution of the mobile mass and the BTC to experimental observations is presented in Sec. V. In Sec. VI we summarize our work and draw conclusions. In the Appendixes we introduce special functions, present details of our calculations, and show additional figures detailing the dynamics encoded in our EMIM.

II. THE EMIM

We depict the motion of tracer particles in the mobile and immobile zones in a one-dimensional two-state model, reflecting the typical situation of particles in a riverbed (or water artery), where the coordinate x measures the distance traveled along the river. Depending on its state, a tracer contributes to either the mobile concentration $C_m(x,t)$ or the immobile concentration $C_{im}(x,t)$. In our model tracers are initially placed in the mobile volume with mobile volume per unit length θ_m in which their motion combines advection and diffusion, mathematically captured by the advection-dispersion operator $L(x) = -v\partial/\partial x + D\partial^2/\partial x^2$ with the advection velocity v [64]. When entering the immobile volume θ_{im} the tracers are immobilized for a duration t drawn from the trapping time PDF $\gamma(t)$, *a priori* of arbitrary shape. We name this model the extended MIM, governed by the transport equations

$$\frac{\partial}{\partial t}C_m(x,t) = -\beta\omega C_m(x,t) + \int_0^t \gamma(t-\tau)\beta\omega C_m(x,\tau)d\tau + L(x)C_m(x,t), \tag{1a}$$

$$\frac{\partial}{\partial t}C_{im}(x,t) = \omega C_m(x,t) - \int_0^t \gamma(t-\tau)\omega C_m(x,\tau)d\tau. \tag{1b}$$

Here ω denotes the mass transfer coefficient and $\beta = \theta_{im}/\theta_m$ the capacity coefficient often used in geophysical contexts. We highlight that this EMIM is based on the two-state, non-Markovian kinetic rate equations for exciton trapping in semiconductors developed in [65] to which we added the advection-dispersion operator.

In this formulation $\gamma(t)$ indeed denotes the trapping time PDF. As can be seen from the relation (1b), particles entering the immobile zone at a previous time $t-\tau$ are released back to the mobile phase with a probability $\gamma(\tau)$. Using the masses

$$M_m(t) = \theta_m \int_{-\infty}^{\infty} dx\, C_m(x,t), \quad M_{im}(t) = \theta_{im} \int_{-\infty}^{\infty} dx\, C_{im}(x,t) \tag{2}$$

in the mobile and immobile zones, respectively, we obtain total mass conservation

$$\frac{d}{dt}[M_m(t) + M_{im}(t)] = 0. \tag{3}$$

We choose the initial condition as the sharp δ peak $C_m(x,0) = M_0/\theta_m\delta(x)$ and $C_{im}(x,0) = 0$, which naturally arises in typical experiments [22,50]. Using the Fourier-Laplace transform,

we obtain from (1) the solution

$$C_m(k,s) = \frac{M_0}{s + \beta\omega[1-\gamma(s)] - ikv + k^2 D} \tag{4}$$

for the mobile concentration, where $f(k,s) = \int_{-\infty}^{\infty}\int_0^{\infty} f(x,t)\exp(-st+ikx)dt\,dx$ denotes the Fourier-Laplace transform of $f(x,t)$, which we solely mark by replacing its arguments. We note that this equation has been previously reported, although without the corresponding equation in the time domain [66]. For the immobile concentration we find

$$C_{im}(k,s) = \omega C_m(k,s)\frac{1-\gamma(s)}{s}. \tag{5}$$

In this two-state approach, when modeling the exchange between the mobile and immobile zones with single-rate first-order mass transfer, exponential long-time decay arises in the BTCs and hence it cannot describe power-law-tailed BTCs [45,67] (see also the discussion below). In the multi-rate mass transfer (MRMT) model, multiple rate coefficients are introduced [49], in which a continuous density of rates following a power-law distribution yields the observed BTCs with a power-law tail [45,67,68]. A distribution of rates occurs in heterogeneous mixtures of layers, cylinders, spheres, or heterogeneous porous sedimentary rock [49,69]. Often, the cumulative function of the trapping time PDF, $\Psi = \int_t^{\infty}\gamma(\tau)d\tau = 1 - \int_0^t \gamma(\tau)d\tau$ [42], is used for the characterization [24], which can, e.g., be reconstructed from a porous medium using x-ray microtomography [27]. If the jump length distribution is independent of the trapping time distribution, the total concentrations of the CTRW and MRMT approaches are indeed equivalent [29,70]. In [45] it was shown that the choice of the power-law form $\Psi(t) = t^{-\mu}/\Gamma(1-\mu)$, with $0 < \mu < 1$, yields a bifractional diffusion-advection equation called fractal MIM [45,71]. In the long-time limit of the fractal MIM the first and second moments of the mobile concentration scale as $\langle x_m\rangle \simeq t^{\mu}$ and $\langle (x_m - \langle x_m\rangle)^2\rangle \simeq t^{2\mu}$, respectively, and reveal superdiffusion for $\mu > 1/2$ and subdiffusion for $\mu < 1/2$, while the mobile particles behave like Brownian particles with drift in the short-time limit [46]. The choice $\Psi(t) = t^{-\mu}/\Gamma(1-\mu)$, however, does not yield a finite value for $\gamma(0)$ and makes γ non-normalizable.

To circumvent this issue, we propose the EMIM (1) that consists of rate equations for both the mobile and immobile concentration. The trapping time in the immobile zone is drawn from the well-defined trapping time PDF which, in contrast to the MIM, is not restricted to an exponential. Our model unifies the following approaches. First, it is an extension of the non-Markovian rate equations used to describe excitons in semiconductors [65] to which we add an advection-dispersion operator. A similar equation exclusively for mobile tracers without advection was presented to describe fine particle deposition in benthic biofilms [52]. Second, we expand the model proposed in [72] in which a particle is mobile for a fixed duration and immobile for a random time drawn from a one-sided Lévy distribution; there, effectively the total concentration is considered and no separate equations are used for mobile and immobile particles. Third, our model corresponds to a model used for particle-tracking simulations [66]. In this work it is argued that the model incorporates waiting time PDFs, and these PDFs are included in the Fourier-Laplace representation. Here we derive and discuss the corresponding rate equations as functions of time and space. Fourth, our model contains the fractal MIM [45] as a special case. When considering the total concentration, i.e., the sum of mobile and immobile concentrations, the fractal MIM is a special case of distributed-order diffusion with a bimodal distribution of fractional orders where the first order is unity and the second ranges between zero. Moreover, we add an advective bias term to this formulation [71].

When rewriting our rate equations in terms of the survival probability, our model matches the MRMT model in [67]. Another set of rate equations involving the immobilization time as a second temporal variable can be found in [73,74]. By choosing a Mittag-Leffler (ML) waiting time PDF our model contains the bifractional solute transport models in [45,71] in the long-time limit, including a power-law decay of the total mobile mass, while retaining a finite value of the memory function in the zero-time limit, $\gamma_{\mathrm{ML}}(0)$. From a physical perspective, the accumulation of immobile particles is similar to particles diffusing in an energy landscape scattered with energetic traps with power-law trapping times [75–77]. We note that while many studies focus on BTCs, some work has been reported regarding the spatial tracer plumes [20,45,78,79]. We address here the question of where the contaminants are in space and how far they spread on average, given a known BTC. Spatial moments of the total concentration and their derivative, the center-of-mass velocity, were, *inter alia*, discussed in [29]. We distinguish here between mobile and immobile distributions, reflecting that in some situations, including the transport dynamics in rivers, only the mobile particles can be detected [22,78]. In [46], approximations for the first five moments are derived, *inter alia*, for the fractal MIM including moments of the mobile plume. Building on such concepts, from our ML waiting time PDF, we obtain explicit expressions for the spatial moments of the mobile, immobile, and total masses.

A. General expressions

We now present the central observables of our model that are calculated as function of a general trapping time PDF.

1. Mobile mass

We set $k = 0$ in Eq. (4) to arrive at the mobile mass in Laplace space. Moreover, we set $\theta_m = 1$ as a unit volume, without loss of generality. We then obtain

$$M_m(s) = \frac{M_0}{s + \beta\omega[1-\gamma(s)]}. \tag{6}$$

The long-time behavior depends on the exact form of the immobilization time PDF, in particular, on whether we have a finite or infinite mean immobilization time. Let us first assume the general waiting time PDF $\gamma_f(t)$ (f denotes finite) with a finite mean $\langle\tau\rangle$. For a small Laplace variable s it can be approximated by $\gamma_f(s) \sim 1 - s\langle\tau\rangle$, which yields the corresponding long-time limit from (6) in terms of the constant value

$$\lim_{t\to\infty} M(t) = \lim_{s\to 0} sM(s) = \frac{M_0}{1+\beta\omega\langle\tau\rangle}, \tag{7}$$

which is consistent with [26,44,66] since $\beta\omega\langle\tau\rangle$ corresponds to the ratio of the time spent in the mobile zone to that in the immobile zone.

For a general PDF $\gamma_d(\tau)$ (d denotes divergent) with diverging mean, we consider its representation for small s with $0 < \mu < 1$ and $\tau_\star > 0$, of the form $\gamma_d(s) \sim 1 - (\tau_\star s)^\mu$, where $\tau_\star$ is a scaling factor, and plug it into the general expression (6), where we look for the long-time limit using the Tauberian theorem [80],

$$\lim_{s\to 0} M(s) \sim \frac{M_0}{\beta\omega\tau_\star^\mu s^\mu} \quad \text{s.t.} \quad \lim_{t\to\infty} M(t) \sim M_0 \frac{t^{\mu-1}}{\beta\omega\tau_\star^\mu \Gamma(\mu)}. \tag{8}$$

We conclude that a waiting time PDF with diverging mean will, remarkably, yield a long-time power-law decay of the mobile mass and thus leave no particles in the mobile zone in the long-time limit, in contrast to a waiting time PDF with finite mean as seen in (7).

2. Moments

From the PDF

$$\begin{aligned}\rho(k,s) &= \frac{1}{M_0}[C_m(k,s) + \beta C_{im}(k,s)] \\ &= \frac{1}{s}\frac{s+\beta\omega[1-\gamma(s)]}{s+\beta\omega[1-\gamma(s)] - ikv + k^2 D}\end{aligned} \tag{9}$$

in Fourier-Laplace space we can calculate the nth moment in Laplace space via

$$\langle x^n(s)\rangle = (-i)^n \frac{\partial^n}{\partial k^n}\rho(k,s)\bigg|_{k=0}. \tag{10}$$

We are interested in the motion of the solute in the mobile phase, as this is the typically accessible experimental quantity [20,22,26,43,52]. Since the mass in the mobile phase changes over time we consider both the unnormalized and the normalized moments, where normalization means dividing the unnormalized moment (denoted by u) (10) by the mobile mass (6) [20,81],

$$\left\langle x_m^n(t)\right\rangle = \langle x^n(t)\rangle_u M_0/M_m(t). \tag{11}$$

We start with the first moment. In the unnormalized form, we have

$$\langle x_m(s)\rangle_u \equiv -i\frac{\partial}{\partial k}\frac{C_m(k,s)}{M_0}\bigg|_{k=0} = \frac{v}{\{s+\beta\omega[1-\gamma(s)]\}^2}. \tag{12}$$

The short-time behavior $\langle x_m(s)\rangle_u = \frac{v}{\{s+\beta\omega[1-\gamma(s)]\}^2} \sim \frac{v}{s^2}$ of this expression can be obtained independently of the trapping time PDF by using the Tauberian theorem for $s \to \infty$ and $\gamma(s) \leqslant 1$, which yields $\langle x\rangle_u(t) = vt$ for small t. This is an expected result, since essentially all mass is mobile at $t = 0$, our initial condition. We obtain

$$\langle x(t)\rangle \overset{t\to 0}{\sim} \langle x_m(t)\rangle_u \overset{t\to 0}{\sim} vt. \tag{13}$$

To assess the long-time behavior we need to know the specific form of the waiting time PDF $\gamma(t)$. We will analyze the long-time behavior for different cases below.

The unnormalized second moment can be calculated analogously,

$$\begin{aligned}\left\langle x_m^2(s)\right\rangle_u &= -\frac{\partial^2}{\partial k^2}\frac{C_m(k,s)}{M_0}\bigg|_{k=0} = \frac{2v^2}{\{s+\beta\omega[1-\gamma(s)]\}^3} \\ &\quad + \frac{2D}{\{s+\beta\omega[1-\gamma(s)]\}^2}.\end{aligned} \tag{14}$$

The corresponding normalized form $\langle x^2(t)\rangle$ follows in the time domain by multiplication with $M_0/M_m(t)$ [Eq. (6)]. The short-time behavior $\langle x^2(s)\rangle_u \sim \frac{2v^2}{s^3} + \frac{2D}{s^2}$ of the second moment can be obtained via the Tauberian theorem for $s \to \infty$ and the above limit form $\gamma(s) \leqslant 1$, which yields $\langle x^2(t)\rangle_u \sim 2Dt + v^2t^2$ at short times. Since the mobile mass is approximately M_0, initially we obtain Brownian motion with advection,

$$\langle x^2(t)\rangle \overset{t\to 0}{\sim} 2Dt + v^2t^2, \tag{15}$$

a result that holds for both $\langle x^2(t)\rangle_u$ and $\langle x^2(t)\rangle$ in this $t \to 0$ limit.

From the general relation (5) between C_m and C_{im} and the nth unnormalized moment (12) we obtain

$$\begin{aligned}\left\langle x_{im}^n\right\rangle_u &= \beta(-i)^n\frac{\partial^n}{\partial k^n}\frac{C_{im}(k,s)}{M_0}\bigg|_{k=0} \\ &= \beta\omega\frac{1-\gamma(s)}{s}(-i)^n\frac{\partial^n}{\partial k^n}\frac{C_m(k,s)}{M_0}\bigg|_{k=0} \\ &= \left\langle x_m^n\right\rangle_u \beta\omega\frac{1-\gamma(s)}{s}.\end{aligned} \tag{16}$$

This quantity describes the spreading of particles in the immobile zone, as they progress by joining the mobile phase and getting absorbed into the immobile zone again. In the expression (16) we notice the factor β that appears when integrating over the immobile domain, i.e., setting $k = 0$, because the immobile domain is larger by this factor than the mobile domain. In addition, we calculate the nth moment of the full concentration using Eq. (9) for $\rho(k,s)$,

$$\langle x^n\rangle = \left\langle x_m^n\right\rangle_u + \beta\left\langle x_{im}^n\right\rangle_u. \tag{17}$$

3. Breakthrough curves

A typical tracer experiment on the field scale records the mobile concentration at a fixed location as a function of time. The obtained statistic is called the breakthrough curve [22,27,28,45,53,54]. When comparing BTCs at different sites with different volumetric fluid discharges Q, it is convenient to analyze the quantity $C \times Q/M_{\text{recov}}$, with the total recovered mass M_{recov} [22]. Inverse Fourier transformation of (4) yields the concentration in the space domain,

$$C_m(x,s) = \frac{\exp\left(\frac{vx}{2D}\right)}{\sqrt{v^2+4\phi(s)D}}\exp\left(-\sqrt{v^2+4\phi(s)D}\frac{|x|}{2D}\right), \tag{18}$$

with $\phi(s) = s + \beta\omega[1-\gamma(s)]$. Its form in the time domain requires an explicit input for $\phi(s)$ (discussed below).

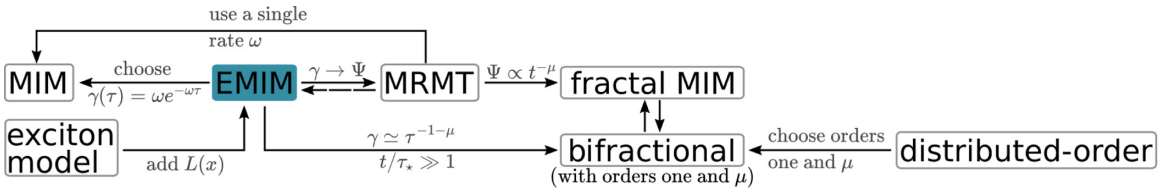

FIG. 2. Relation between different transport models. The EMIM follows from the exciton model [65] by adding the transport operator $L(x)$. The EMIM contains the MIM as a special case for $\gamma(\tau) = \omega e^{-\omega\tau}$, as shown in Sec. III A. Using the cumulative Ψ probability function of γ, the EMIM can be rewritten as an MRMT model, as presented in Sec. IV. Going the opposite direction requires $\Psi(0) = 1$. If $\Psi \propto \tau^{-\mu}$, the MRMT model is equivalent to the fractal MIM [45]. The full concentration follows a bifractional diffusion equation. The latter arises directly from the EMIM in the long-time limit, when the waiting time PDF asymptotically behaves like $\tau^{-1-\mu}$. The bifractional diffusion equation is a special case of distributed-order diffusion where instead of a continuous distribution the values one and μ for the diffusion exponents are chosen.

III. EMIM DYNAMICS FOR SPECIFIC TRAPPING PDFS

We now obtain explicit forms for the characteristic observables in the EMIM dynamics for exponential and ML-type trapping time density functions and discuss possible extensions of our model.

A. Exponential trapping time distribution

We start with the choice of an exponential distribution for the trapping time PDF,

$$\gamma(\tau) = \omega e^{-\omega\tau}, \tag{19}$$

with mean $\langle\tau\rangle = 1/\omega$. The variable ω is identical to the mass transfer coefficient from the rate equations (1). In the following, we demonstrate three implications of this choice. First, when choosing an exponential distribution in the EMIM the mobile concentration reflects one state of a general Markovian two-state model. Second, it follows immediately that matching ω with the mass transfer coefficient from our rate equations (1) is not a restriction when only considering mobile tracers. Hence, we make this choice in (19). Third, we show the equivalence of both EMIM rate equations with the choice (19) in the model of [26].

To this end let us consider a general Markovian two-state MIM with immobilization rate ω_1 and remobilization rate ω_2 as discussed in [65],

$$\begin{aligned}\frac{\partial}{\partial t}C_m &= -\omega_1 C_m + \omega_2 C_{im} + L(x)C_m,\\ \frac{\partial}{\partial t}C_{im} &= \omega_1 C_m - \omega_2 C_{im},\end{aligned} \tag{20}$$

where we added the advection-diffusion operator $L(x)$ to the mobile rate equation. From (20) with the initial conditions $C_{im}(x,0) = 0$ and $C_m(x,0) = M_0\delta(x)$ we obtain the formal solution [65]

$$C_{im}(x,t) = \int_0^t \omega_1 e^{-\omega_2(t-\tau)} C_m(x,\tau)d\tau. \tag{21}$$

We insert this solution into (20) to find

$$\begin{aligned}\frac{\partial}{\partial t}C_m(x,t) = -\omega_1 C_m(x,t) + \omega_1\int_0^t \omega_2 e^{-\omega_2(t-\tau)} C_m(x,\tau)d\tau\\ + L(x)C_m(x,t).\end{aligned} \tag{22}$$

If we now replace ω_2 with ω and ω_1 with $\beta\omega$, we recover the mobile rate equation of the EMIM (1a) with the specific choice (19). The rate equation for the immobile concentration,

$$\frac{\partial}{\partial t}C_{im}(x,t) = \beta\omega C_m(x,t) - \beta\int_0^t \gamma(t-\tau)\omega C_m(x,\tau)d\tau, \tag{23}$$

differs from our immobile rate equation (1b) only by the factor β. Note that the equivalence of the mobile concentrations suffices because C_{im} is typically not measured. We can repeat the same steps with the rate equations, which are equivalent to the model proposed in [26],

$$\frac{\partial C_m}{\partial t} + \beta\frac{\partial C_{im}}{\partial t} = L(x)C_m, \tag{24a}$$

$$\frac{\partial C_{im}}{\partial t} = \omega(C_m - C_{im}), \tag{24b}$$

for which we obtain

$$\frac{\partial}{\partial t}C_{im}(x,t) = \omega C_m(x,t) - \int_0^t \omega e^{-\omega(t-\tau)} C_m(x,\tau)d\tau. \tag{25}$$

Note specifically the equivalence with both our mobile and immobile rate equations (1), as can be seen from inserting (25) in (24a). Equations (24) are first-order rate equations. Therefore, we refer to the choice $\gamma(\tau) = \omega\exp(-\omega\tau)$ as the first-order model or simply exponential model. Figure 2 visualizes the relation of the EMIM to the MIM and other models.

In the long-time limit corresponding to $s \to 0$ in Laplace space, the mobile concentration is equal to the immobile concentration, as we show in the following calculation starting from the general relation (5) between C_{im} and C_m:

$$\begin{aligned}\lim_{s\to 0} C_{im}(k,s) &= \lim_{s\to 0}\omega C_m(k,s)\frac{1-\frac{\omega}{s+\omega}}{s}\\ &= \lim_{s\to 0}\frac{\omega}{s+\omega}C_m(k,s) = \lim_{s\to 0} C_m(k,s).\end{aligned} \tag{26}$$

Therefore, it suffices to calculate the long-time limits of the normalized moments of the mobile concentration to obtain the long-time limits of the moments of the immobile and full concentrations. Note that, due to different mobile and immobile volumes, the respective masses differ, which, however, does not restrict generality.

1. Mobile mass

Inverse Laplace transformation of the mobile mass (6) yields

$$M_m(t) = \frac{M_0}{1+\beta}(1+\beta e^{-\omega(1+\beta)t}), \text{ and thus}$$
$$\lim_{t\to\infty} M_m(t) = \frac{M_0}{1+\beta} \tag{27}$$

in the long-time limit, in accordance with (7) with $\langle\tau\rangle = 1/\omega$.

2. Moments

Using the general equation (12) for $\langle x_m(s)\rangle_u$, we obtain the result for the unnormalized first moment in time domain through inverse Laplace transformation,

$$\langle x_m(t)\rangle_u = \frac{vt}{(1+\beta)^2}(1+\beta^2 e^{-\omega(1+\beta)t}) + v\frac{2\beta}{(1+\beta)^3\omega}(1-e^{-\omega(1+\beta)t}), \tag{28}$$

from which we find the long-time behavior

$$\langle x_m(t)\rangle_u \overset{t\to\infty}{\sim} \frac{vt}{(1+\beta)^2}. \tag{29}$$

We divide (28) by the mobile mass for normalization,

$$\langle x_m(t)\rangle = \frac{vt}{(1+\beta)}\frac{1+\beta^2 e^{-\omega(1+\beta)t}}{1+\beta e^{-\omega(1+\beta)t}} + v\frac{2\beta}{(1+\beta)^2\omega}\frac{1-e^{-\omega(1+\beta)t}}{1+\beta e^{-\omega(1+\beta)t}}, \tag{30}$$

and find the corresponding long-time behavior

$$\langle x_m(t)\rangle \overset{t\to\infty}{\sim} \frac{vt}{1+\beta}. \tag{31}$$

The normalization thus corresponds to rescaling time as $t \to t/(1+\beta)$.

After Laplace inversion of (14) we find the unnormalized second moment valid at all times,

$$\langle x_m^2(t)\rangle_u = \frac{2v^2}{(1+\beta)^3}\left[t^2\left(\frac{1}{2}+\frac{\beta^3}{2}e^{-(1+\beta)\omega t}\right) + t\frac{3\beta}{(1+\beta)\omega}(1-\beta e^{-(1+\beta)\omega t}) + \frac{3(\beta^2-\beta)}{(1+\beta)^2\omega^2}\left(1-e^{-(1+\beta)\omega t}\right)\right] + 2D\frac{t}{(1+\beta)^2}(1+\beta^2 e^{-(1+\beta)\omega t}) + 2D\frac{2\beta}{(1+\beta)^3\omega}(1-e^{-(1+\beta)\omega t}), \tag{32}$$

and after normalizing with $M_m(t)$ [expression (27)], we obtain the normalized second mobile moment

$$\langle x_m^2(t)\rangle = \frac{2v^2}{(1+\beta)^2(1+\beta e^{-(1+\beta)\omega t})}\left[t^2\left(\frac{1}{2}+\frac{\beta^3}{2}e^{-(1+\beta)\omega t}\right) + t\frac{3\beta}{(1+\beta)\omega}(1-\beta e^{-(1+\beta)\omega t}) + \frac{3(\beta^2-\beta)}{(1+\beta)^2\omega^2}(1-e^{-(1+\beta)\omega t}\right] + 2D\frac{t}{(1+\beta)}\frac{1+\beta^2 e^{-(1+\beta)\omega t}}{1+\beta e^{-(1+\beta)\omega t}} + 2D\frac{2\beta}{(1+\beta)^2\omega}\frac{1-e^{-(1+\beta)\omega t}}{1+\beta e^{-(1+\beta)\omega t}}. \tag{33}$$

In the long-time limit $t \gg 1/(1+\beta)\omega$ we find from (32) that

$$\langle x_m^2(t)\rangle_u \overset{t\to\infty}{\sim} \frac{v^2}{(1+\beta)^3}t^2 + 2D\frac{t}{(1+\beta)^2}. \tag{34}$$

When we account for the change of mobile mass, we obtain

$$\langle x_m^2(t)\rangle \overset{t\to\infty}{\sim} \frac{v^2}{(1+\beta)^2}t^2 + 2D\frac{t}{1+\beta}, \tag{35}$$

which, as for the first moment, corresponds to rescaling time $t \to t/(1+\beta)$ [see the relation (69) in [45]]. In fact, the expression (35) in terms of $t/(1+\beta)$ is exactly the expected combination of advection and diffusion of a Brownian particle in a drift flow v, $v^2t^2 + 2Dt$.

In the long-time limit we obtain the second central moment for the classical model in the form

$$\langle (x-\langle x\rangle)^2\rangle \overset{t\to\infty}{\sim} 2\frac{D}{1+\beta}t, \tag{36}$$

which grows linearly and corresponds to free Brownian motion with rescaled time $t \to t/(1+\beta)$. These results coincide with those reported in [79].

3. Breakthrough curves

We finally calculate the long-time behavior of the mobile concentration $C_m(x,t)$, whose interpretation at a fixed point x is that of the BTC. Starting from the general expression (18) for $C_m(k,s)$, we find for a small Laplace variable s that $\phi \sim s(1+\beta)$. Fourier-Laplace inversion to the space-time domain yields the expected Gaussian form

$$C_m(x,t) \sim \frac{M_0}{1+\beta}\sqrt{\frac{1+\beta}{4\pi Dt}}\exp\left(-\left[x-\frac{vt}{1+\beta}\right]^2\frac{1+\beta}{4Dt}\right). \tag{37}$$

This result quantifies the concentration of a free Brownian particle with rescaled time $t \to t/(1+\beta)$. Note that the immobile concentration has the same long-time limit as shown in (26).

B. Mittag-Leffler trapping time distribution

We now turn to the case when the characteristic trapping time becomes infinite and, as an explicit form, choose the generalized or two-parametric ML trapping time PDF [82,83]

$$\gamma_{\rm ML}(t) = \frac{(t/\tau_\star)^\mu}{t}E_{\mu,\mu}(-[t/\tau_\star]^\mu), \tag{38}$$

with $0 < \mu < 1$ and $\tau_\star > 0$. This distribution has the power-law tail $\simeq t^{-1-\mu}$ that indeed produces a diverging mean. We refer to the choice (38) as the ML model in the following. The corresponding PDF in the Laplace domain reads [84]

$$\gamma_{\rm ML}(s) = \frac{1}{1+(\tau_\star s)^\mu}. \tag{39}$$

In Sec. IV we show that the dynamics of the total tracer concentration in our model is a particular case of the bifractional diffusion equation [71], to which a transport term is added, and the fractal model [45], in the long-time limit $t \gg \tau_\star$. We note that another common choice for a PDF with a power-law tail is the one-sided Lévy distribution [34,65,71]. While the latter is supported formally by the generalized central limit theorem [85], its more intricate Laplace transform $\exp[-(\tau_\star s)^\mu]$ renders analytical calculations virtually impossible. As the results are expected to be very close to those of the ML model, we use the more easily tractable ML PDF as the basis for our further study.

1. Mobile mass decay

For the mobile mass $M_m(s)$ [see the expression (6)], we obtain in Appendix A that

$$M_m(t) = M_0 e^{-\beta\omega t} + M_0 \beta\omega\tau_\star^\mu t \sum_{k=1}^{\infty} (-1)^{k+1} \left(\frac{t}{\tau}\right)^{\mu k} \times E_{1,\mu k+2}^{k+1}(-\beta\omega\tau_\star^\mu t), \tag{40}$$

which yields the short-time behavior

$$M_m(t) \sim M_0(1-\beta\omega t) + M_0 \frac{\beta\omega t}{\Gamma(\mu+2)} \left(\frac{t}{\tau_\star}\right)^\mu + O(t^\alpha). \tag{41}$$

Here the first term contains the initial mobile mass and immobilization with rate $\beta\omega$. The second term contains the lowest order of the tracer remobilization proportional to $t^{1+\mu}$. The Landau symbol $O(\cdot)$ here represents higher-order terms with $\alpha = \min(1+2\mu, 2)$. Note that the series (40) converges relatively slowly in numerical implementations.

We calculate the long-time limit of the mobile mass from its Laplace representation. For $t \to \infty$, corresponding to $s \to 0$, we can approximate $\gamma_{\rm ML} \sim 1 - (\tau_\star s)^\mu$. We plug this form into the general expression of $M_m(s)$ [Eq. (6)] and find $M_m(s) \sim \frac{M_0}{\beta\omega\tau_\star^\mu s^\mu}$ for $s \ll 1/\tau_\star$. Via the Tauberian theorem, we obtain the result in the time domain,

$$M_m \overset{t\to\infty}{\sim} M_0 \frac{t^{\mu-1}}{\beta\omega\tau_\star^\mu \Gamma(\mu)}, \tag{42}$$

in agreement with result (8).

2. Moments

We calculate the long-time limits of the moments using the same approximation $\gamma(s)_{\rm ML} \sim 1 - (\tau_\star s)^\mu$ for $t \to \infty$ as for the mobile mass asymptotes. Using the general formula (12) for the first unnormalized moment in Laplace space, we find

$$\langle x_m\rangle_u = i\frac{\partial}{\partial k}\frac{C_m(s)}{M_0}\bigg|_{k=0} = \frac{v}{(s+\beta\omega\tau_\star^\mu s^\mu)^2} = \frac{v}{s^2 + 2\beta\omega\tau_\star^\mu s^{1+\mu} + \beta^2\omega^2\tau_\star^{2\mu} s^{2\mu}} \overset{s\to 0}{\sim} \frac{v}{\beta^2\omega^2\tau_\star^{2\mu} s^{2\mu}}. \tag{43}$$

In the last step, we used that $0 < \mu < 1$. This corresponds to

$$\langle x_m\rangle_u \overset{t\to\infty}{\sim} v\frac{t^{2\mu-1}}{\beta^2\omega^2\tau_\star^{2\mu}\Gamma(2\mu)}. \tag{44}$$

We now turn to the normalized first moment for large $t \to \infty$ and take the quotient of (44) and (42), namely,

$$\langle x_m\rangle \overset{t\to\infty}{\sim} \frac{v\frac{t^{2\mu-1}}{\beta^2\omega^2\tau_\star^{2\mu}\Gamma(2\mu)}}{\frac{t^{\mu-1}}{\beta\omega\tau_\star^\mu\Gamma(\mu)}} = \frac{vt^\mu}{\beta\omega\tau_\star^\mu}\frac{\Gamma(\mu)}{\Gamma(2\mu)}. \tag{45}$$

The asymptote of the first moment is hence nonlinear, similar to the subdiffusive CTRW case [14].

To obtain the asymptote of the first moment from the immobile concentration, we start from the general relation (16) between $\langle x_m^n\rangle_u$ and $\langle x_{im}^n\rangle_u$ for $n = 1$, obtaining, for $s \to 0$,

$$\langle x_{im}\rangle_u = \omega\beta v \frac{1}{\{s+\beta\omega[1-\gamma(s)]\}^2}\frac{1-\gamma(s)}{s} = \omega\beta v \frac{\tau_\star^\mu s^{\mu-1}}{(s+\beta\omega\tau_\star^\mu s^\mu)^2} \overset{s\to 0}{\sim} v\frac{s^{-\mu-1}}{\beta\omega\tau_\star^\mu}, \tag{46}$$

which in the time domain corresponds to

$$\langle x_{im}\rangle \overset{t\to\infty}{\sim} \frac{vt^\mu}{\beta\omega\tau_\star^\mu\Gamma(1+\mu)}. \tag{47}$$

Note that in the long-time limit all mass is immobile and hence we do not need to normalize the moment. This result differs from $\langle x_m\rangle$ only by the factor $\Gamma(2\mu)/\Gamma(\mu)\Gamma(1+\mu)$, which is unity for $\mu = 1$ and larger than unity for $0 < \mu < 1$. Thus, the mobile particles travel further on average than the immobile particles in the long-time limit, as it should be.

In what follows, we restrict ourselves to the mobile moments. Calculations of higher immobile moments are fully analogous to the mobile moments and the first immobile moment.

Let us turn to the second unnormalized mobile moment for $s \to 0$,

$$\langle x_m^2\rangle_u = -\frac{\partial^2}{\partial k^2}\frac{C_m(s)}{M_0}\bigg|_{k=0} \overset{s\to 0}{\sim} \frac{2D}{\beta^2\omega^2\tau_\star^{2\mu}s^{2\mu}} + \frac{2v^2}{\beta^3\omega^3\tau_\star^{3\mu}s^{3\mu}}. \tag{48}$$

This corresponds, in the time domain, to

$$\langle x_m^2\rangle_u \overset{t\to\infty}{\sim} 2D\frac{t^{2\mu-1}}{\beta^2\omega^2\tau_\star^{2\mu}\Gamma(2\mu)} + 2v^2\frac{t^{3\mu-1}}{\beta^3\omega^3\tau_\star^{3\mu}\Gamma(3\mu)}. \tag{49}$$

Let us look at the normalized second moment for long t and take the quotient of (49) and (42), namely,

$$\langle x_m^2\rangle \overset{t\to\infty}{\sim} \frac{2D\frac{t^{2\mu-1}}{\beta^2\omega^2\tau_\star^{2\mu}\Gamma(2\mu)} + 2v^2\frac{t^{3\mu-1}}{\beta^3\omega^3\tau_\star^{3\mu}\Gamma(3\mu)}}{\frac{t^{\mu-1}}{\beta\omega\tau_\star^\mu\Gamma(\mu)}} = 2D\Gamma(\mu)\frac{t^\mu}{\beta\omega\tau_\star^\mu\Gamma(2\mu)} + 2v^2\Gamma(\mu)\frac{t^{2\mu}}{\beta^2\omega^2\tau_\star^{2\mu}\Gamma(3\mu)}. \tag{50}$$

If only mobile tracers can be observed and the waiting time PDF does not depend on β or ω, the parameters β and ω cannot be determined individually, because they only appear as the product $\beta\omega$ in the Fourier-Laplace solution (4) of $C_m(k,s)$ and all quantities derived therefrom. Additionally, in the long-time limits of the ML model the parameter $\tau_\star$ solely appears in the product $\beta\omega\tau_\star^\mu$ and hence cannot be determined separately. When only the long-time behavior of the mobile

tracers is known, it therefore makes sense to only consider the parameter $\beta_s' = \beta\omega\tau_\star^\mu$. At intermediate times, the parameter $\tau_\star$ can be obtained independently of $\beta\omega$, as the mobile mass (40) shows for the ML model.

Using the asymptotes (45) and (50) of the first and second moments, we obtain the second central moment

$$\langle [x_m(t) - \langle x_m(t)\rangle]^2\rangle = 2D\Gamma(\mu)\frac{t^\mu}{\beta\omega\tau_\star^\mu\Gamma(2\mu)} + v^2\Gamma(\mu)\frac{t^{2\mu}}{(\beta\omega\tau_\star^\mu)^2}\left(\frac{2}{\Gamma(3\mu)} - \frac{\Gamma(\mu)}{\Gamma^2(2\mu)}\right). \quad (51)$$

The expression in the large parentheses only vanishes for $\mu = 1$. In the long-time limit, the second central moment hence behaves as $t^{2\mu}$, i.e., subdiffusively for $0 < \mu < 1/2$ and superdiffusively for $1/2 < \mu < 1$. The occurrence of a superdiffusive behavior in a process dominated by a scale-free waiting time PDFs is known for subdiffusive CTRW processes with drift [35]. The phenomenon stems from the fact that the process has a strong memory of the initial position, its amplitude decaying only as $\simeq t^{-\mu}$. Concurrently, the mobile particles are advected, thus creating a highly asymmetric position PDF of the process. In fact, while for a Brownian particle the ratio of standard deviation to mean position decays as $\simeq t^{-1/2}$, for the subdiffusive particle the ratio is asymptotically constant, reflecting the large particle spread [35]. This behavior is also witnessed by the slope of the concentration profiles discussed below.

3. Breakthrough curves

In Appendix B we calculate the long-time limit of the mobile concentration using the special function of Wright type M_μ (Mainardi function) [84],

$$M_\mu(z) = \sum_{n=0}^{\infty}\frac{(-z)^n}{n!\Gamma[-\mu n + (1-\mu)]}. \quad (52)$$

From the general equation for $C_m(x,s)$ [Eq. (18)] we find in the limit $s \ll (v^2/4\beta\omega\tau_\star^\mu D)^{1/\mu}$ for $v > 0$, using the Laplace inversion (B3),

$$C_m(x,t) \sim \frac{\beta\omega\tau_\star^\mu\mu}{v^2}\exp\left(\frac{v}{2D}(x-|x|)\right)|x|t^{-1-\mu}M_\mu \times \left(\frac{\beta\omega\tau_\star^\mu}{v}|x|t^{-\mu}\right). \quad (53)$$

For long times $t \gg \tau_\star(\frac{\beta\omega}{v}|x|)^{1/\mu}$ the argument of M_μ in (53) goes to zero. With the limit $M_\mu(z) \sim 1$ for $z \to 0$, we thus have the asymptotic scaling $C_m \simeq t^{-1-\mu}$ for fixed x. In the long-time limit, we find the immobile concentration profile using the Laplace inversion (B4),

$$C_{im}(x,t) \sim \frac{\beta\omega\tau_\star^\mu}{v}\exp\left(\frac{v}{2D}(x-|x|)\right)t^{-\mu}M_\mu\left(\frac{\beta\omega\tau_\star^\mu}{v}|x|t^{-\mu}\right). \quad (54)$$

Equations (53) and (54) clearly show exponential cutoffs for $x < 0$, i.e., a strong suppression against the direction of the advection, as it should be. For $x > 0$ the exponential function in Eq. (54) vanishes and a cusp emerges. Conversely, at short times and fixed x we find a Gaussian expression of C_m.

C. Comparison of the two EMIM cases

When choosing an exponential trapping time distribution, our model follows the dynamic equations (24) corresponding to the first-order mass transfer model (24) [26]. In the long-time limit the mobile and immobile concentrations are equal and the mass fraction $1/(1+\beta)$ remains mobile. The unnormalized and normalized moments remain unchanged except for the rescaled time $t \to t/(1+\beta)$. In the ML model, the diverging mean trapping time leads to different mobile and immobile concentrations and a power-law decay of the mobile mass. The first and second moments grow nonlinearly and nonquadratically in time, respectively. The second central moment shows anomalous diffusion, i.e., subdiffusion for $0 < \mu < 1/2$ and superdiffusion for $1/2 < \mu < 1$. All long-time limiting behaviors are summarized in Table I. In Appendix E we validate our results with particle-tracking simulations.

D. Tempered power-law and composite models

The ML model features a diverging characteristic trapping time. While in many cases such models reveal adequate descriptions (e.g., in [40,41] in which fits with a γ function reveal a cutoff at the very end of the experimental window) in other cases experiments explore time ranges in which the finiteness of the system becomes significant. A finite system size implies a finite number of locations, e.g., pores, where the tracers can immobilize. This implies that a finite waiting time exists, which has been measured, e.g., for dye dispersion in a saturated sand pack [69]. A typical approach is to introduce an exponential cutoff in the power-law waiting time PDF of the form [22,29,31,52,69]

$$\gamma_t(t) = \frac{\exp(-t/\tau_t)}{\gamma(s = 1/\tau_t)}\gamma(t), \quad (55)$$

with the characteristic crossover time $\tau_t > 0$. An interesting case is reported in [54] for which τ_t increases with biofilm growth. In Laplace space we find

$$\gamma_t(s) = \frac{\gamma(s + 1/\tau_t)}{\gamma(s = 1/\tau_t)}. \quad (56)$$

If we choose the ML model as a special example, the associated tempered PDF has the characteristic waiting time

$$\langle t\rangle = \frac{\tau_\star^\mu\mu}{\tau_t^{\mu-1}[1 + (\tau_\star/\tau_t)^\mu]}. \quad (57)$$

Together with the general limit (7) of $M_m(t)$ we find

$$\lim_{t\to\infty} M_m(t) = \frac{M_0}{1 + \beta\omega\frac{\tau_\star^\mu\mu}{\tau_t^{\mu-1}(1+\tau_\star^\mu\tau_t^{-\mu})}}. \quad (58)$$

The assumption $\tau_t \gg \tau_\star$ appears reasonable; therefore, the short-time expansion of the mobile mass coincides with the untempered ML model (41).

We now calculate an estimation of $M_m(t)$ for $\tau_\star \ll t \ll \tau_t$ using γ_t (56) and the general formula for M_m (6) in Laplace

TABLE I. Main long-time behavior of the mobile-immobile moments with section and equation numbers. At short times, regardless of the trapping time PDF, we have $\langle x_m\rangle \approx vt$ and $\langle x_m^2\rangle \approx v^2t^2 + 2Dt$, due to $C_m(x,0) = M_0\delta(x)$ and $C_{im}(x,0) = 0$.

Moment	Long-time behavior, mobile phase	Long-time behavior, immobile phase
	Exponential model (Sec. III A)	
$M_m(t)/M_0$	$\frac{1}{1+\beta}$ [Eq. (27)]	
$\langle x\rangle$	$\frac{vt}{1+\beta}$ [Eq. (31)]	
$\langle x^2\rangle$	$2D\frac{t}{1+\beta} + \frac{v^2t^2}{(1+\beta)^2}$ [Eq. (35)]	
$\langle (x-\langle x\rangle)^2\rangle$	$2D\frac{t}{1+\beta}$ [Eq. (36)]	
$C_{m,im}(x,t)$	$C_{m,im}(x,t) = \frac{M_0}{\sqrt{\frac{2Dt}{1+\beta}}}\exp[-(x-\frac{vt}{1+\beta})^2\frac{1}{4Dt/(1+\beta)}]$ [Eq. (37)]	
	ML model (Sec. III B)	
$M_{m,im}(t)/M_0$	$\frac{t^{\mu-1}}{\beta\omega\tau_\star^\mu\Gamma(\mu)}$ [Eq. (42)]	
$\langle x_{m,im}\rangle$	$v\Gamma(\mu)\frac{t^\mu}{\beta\Gamma(\mu)}$ [Eq. (45)]	$\frac{vt^\mu}{\beta\omega\tau_\star^\mu\Gamma(1+\mu)}$ [Eq. (47)]
$\langle x_{m,im}^2\rangle$	$\frac{t^\mu 2D\Gamma(\mu)}{\beta\Gamma(2\mu)} + \frac{t^{2\mu}2v^2\Gamma(\mu)}{\beta^2\omega^2\tau_\star^{2\mu}\Gamma(3\mu)}$ [Eq. (50)]	
$\langle (x_{m,im}-\langle x_{m,im}\rangle)^2\rangle$	$\frac{t^\mu 2D\Gamma(\mu)}{\beta\omega\tau_\star^\mu\Gamma(2\mu)} + \frac{t^{2\mu}v^2\Gamma(\mu)}{(\beta\omega\tau_\star^\mu)^2}(\frac{2}{\Gamma(3\mu)} - \frac{\Gamma(\mu)}{\Gamma^2(2\mu)})$ [Eq. (51)]	
$C_{m,im}(x,t)$	$\frac{\beta\omega\tau_\star^\mu\mu}{v^2}e^{\frac{v}{2D}(x-\lvert x\rvert)}\frac{\lvert x\rvert}{t^{1+\mu}}M_\mu(\frac{\beta\omega\tau_\star^\mu}{v}\lvert x\rvert t^{-\mu})$ [Eq. (53)]	$\frac{\beta\omega\tau_\star^\mu}{vt^\mu}e^{\frac{v}{2D}(x-\lvert x\rvert)}M_\mu(\frac{\beta\omega\tau_\star^\mu}{v}\lvert x\rvert t^{-\mu})$ [Eq. (54)]

space,

$$M_m(s') = \frac{M_0}{s' - \frac{1}{\tau_t} + \beta\omega\left(1 - \frac{1}{1+(\tau_\star s')^\mu} - \frac{\tau_\star^\mu\tau_t^{-\mu}}{1+(\tau_\star s')^\mu}\right)}, \tag{59}$$

where we define $s' = s + 1/\tau_t$. This definition allows us to analyze (59) for small s',

$$M_m(s') \overset{s'\to 0}{\sim} \frac{M_0}{\beta\omega[(\tau_\star s')^\mu(1+\tau_\star^\mu\tau_t^{-\mu}) - \tau_\star^\mu\tau_t^{-\mu}] - \frac{1}{\tau_t}} \tag{60}$$

$$\sim \frac{M_0}{\beta\omega\tau_\star^\mu(1+\tau_\star^\mu\tau_t^{-\mu})}\frac{1}{s^\mu - \frac{\tau_\star^\mu\tau_t^{-\mu} + (\tau_t\beta\omega)^{-1}}{\tau_\star^\mu + \tau_\star^{2\mu}\tau_t^{-\mu}}} \tag{61}$$

and thus, after Laplace inversion [see [84], Eq. (4.10.1)],

$$M_m(t) \sim \frac{M_0}{\beta\omega\tau_\star^\mu(1+\tau_\star^\mu\tau_t^{-\mu})}t^{\mu-1}E_{\mu,\mu}(\lambda t^\mu), \tag{62}$$

with $\lambda = [\tau_\star^\mu\tau_t^{-\mu} + (\tau_t\beta\omega)^{-1}]/[\tau_\star^\mu + \tau_\star^{2\mu}\tau_t^{-\mu}]$. Since we have $\tau_t \gg \tau_\star$, λ simplifies to $\lambda = 1/\tau_\star^\mu\tau_t\beta\omega$. Using $\mathscr{L}^{-1}\{f(s+1/\tau_t)\} = \exp(-t/\tau_t)f(t)$, we find

$$M_m(t) \sim \frac{M_0}{\beta\omega\tau_\star^\mu(1+\tau_\star^\mu\tau_t^{-\mu})}t^{\mu-1}E_{\mu,\mu}(\lambda t^\mu), \quad \tau_\star \ll t \ll \tau_t. \tag{63}$$

Another class of modification to the models considered above arises for the case of composite systems, in which two distinct immobile zones with different trapping time PDFs $\gamma_1(\tau)$ and $\gamma_2(\tau)$ exist. Analogously to (1), these systems are described by

$$\frac{\theta_m}{\theta_{im}}\frac{\partial}{\partial t}C_m(x,t) = -\omega C_m(x,t) + \int_0^t [b\gamma_1(t-\tau) + (1-b) \times \gamma_2(t-\tau)]\omega C_m(x,t)d\tau + \frac{\theta_m}{\theta_{im}}L(x)C_m(x,t), \tag{64a}$$

$$\frac{\partial}{\partial t}C_{im,1}(x,t) = b\omega C_m(x,t) - \int_0^t b\gamma_1(t-\tau)\omega C_m(x,t)d\tau, \tag{64b}$$

$$\frac{\partial}{\partial t}C_{im,2}(x,t) = (1-b)\omega C_m(x,t) - \int_0^t (1-b)\gamma_2(t-\tau)\omega C_m(x,t)d\tau. \tag{64c}$$

Here the particle immobilizes into the first immobile zone with probability b and into the second zone otherwise. The combination of two remobilization processes arises, for instance, in intragranular diffusion processes, where mesopores and micropores are present and the latter lead to slow diffusion with γ-distributed diffusion rates [51]. We are mainly interested in the mobile zone; consequently, we define

$$\gamma(\tau) = b\gamma_1(\tau) + (1-b)\gamma_2(\tau) \tag{65}$$

and consider (1a) only. All observables can be obtained by plugging the corresponding (composite) trapping time PDFs into the general expressions that we presented in Sec. II A and numerically calculating the Laplace inversion (see the explicit results in Sec. V A). We note that we calculate all Laplace inversions using the implementation of the de Hoog method [86] using the PYTHON package MPMATH [87].

IV. CONNECTION TO FRACTIONAL MODELS

We now proceed to show that the EMIM formalism developed here is consistent with the bifractional diffusion equation model [71] and the fractal MIM presented in [45] in the limit $t \gg \tau_\star$. The relations between these models and the EMIM are outlined in Fig. 2.

A. Connection to bifractional diffusion equation and fractal MIM

To this end, we recall our definition of the cumulative function of the waiting time PDF, $\Psi(t) = \int_t^\infty \gamma(\tau)d\tau$, i.e., the survival probability in the trapped state. Since $\int_0^\infty \gamma(\tau)d\tau = 1$, we have $1 - \Psi(t) = \int_0^t \gamma(\tau)d\tau$. From here we obtain $\gamma(\tau) = -\partial\Psi(t)/\partial t$ and $\Psi(s) = [1-\gamma(s)]/s$. Now we aim at

rewriting the dynamic equations (1) of the EMIM in terms of this survival probability. We start with the relation (1a) and use integration by parts in the second term of the right-hand side,

$$\int_0^t \gamma(t-\tau)C_m(x,t)d\tau = \Psi(t)C_m(0) + \Psi(0)C_m(t) - \int_0^t d\tau \Psi(t-\tau)\frac{d}{d\tau}C_m(\tau). \tag{66}$$

Thus, our model (1a) is equivalent to

$$\frac{\partial}{\partial t}C_m(t) + \beta\omega\int_0^t \Psi(t-\tau)\frac{\partial C_m(\tau)}{\partial \tau}d\tau = -\beta\omega\Psi(t)C_m(0) + L(x)C_m(x,t). \tag{67}$$

Now, for our ML model $\gamma(s) = 1/[1+(\tau_\star s)^\mu]$ the survival probability in the Laplace domain reads

$$\Psi(s) = \frac{s^{\mu-1}\tau_\star^\mu}{1+(\tau_\star s)^\mu}. \tag{68}$$

Thus, in our approach $\Psi(t) = E_\mu[-(t/\tau_\star)^\mu] \to e^{-t/\tau_\star}$ for $\mu = 1$. The ML function converges to unity when $t \to 0$ and decays as the power law $t^{-\mu}\tau_\star^\mu/\Gamma(1-\mu)$ at large t. If we only retain the long-time asymptotes we arrive at the model in [45] in terms of the fractional Caputo derivative of order $0 < \mu < 1$ [88].

For the specific choice $\Psi(t) = \omega e^{-\omega t}$ the fractal model in [45] leads to the classical mass transfer model (24a). Note that this choice is equivalent to our exponential model with $\gamma(t) = \omega e^{-\omega t}$. It leads to the linear retardation factor $(1+\beta)$ [45] and the dynamic equation

$$(1+\beta)\frac{\partial C_{\rm tot}}{\partial t} = L(x)C_{\rm tot}, \quad C_{\rm tot}(x,0) = \theta_m C_{m,0}(x) \tag{69}$$

for the total concentration that we also found in the long-time limit of our exponential model. In this sense our approach is fully consistent with the fractal MIM developed in [45]. However, in our EMIM formulation the trapping time distribution $\gamma(t)$ is a proper PDF including the case of PDFs with diverging mean; in particular, no divergence at $\gamma(0)$ occurs.

We proceed to analyze the connection of the EMIM to the bifractional diffusion equation. In the long-time limit we can rewrite the total concentration (9) using a ML PDF and the approximation $\gamma(s) = 1 - \tau_\star^\mu s^\mu$ to obtain

$$sC_{\rm tot}(k,s) - M_0 + \beta\omega\tau_\star^\mu s^\mu C_{\rm tot}(k,s) - M_0\beta\omega\tau_\star^\mu s^{\mu-1} = (ikv - k^2D)C_{\rm tot}(k,s). \tag{70}$$

We can now identify a first-order derivative and a Caputo fractional derivative, yielding in the time-space domain

$$\frac{\partial C_{\rm tot}}{\partial t} + \beta_s'\frac{\partial^\mu C_{\rm tot}}{\partial t^\mu} = L(x)C_{\rm tot}, \tag{71}$$

which is a bifractional diffusion equation, as discussed in [71,72,89] and reported in [45] for $\theta_m C_{m,0}(x) = C_{\rm tot}(x,0)$, with a generalized transport operator $L(x)$.

B. Analytical forms of the transport moments

For a small Laplace variable s the Laplace transform of the ML PDF behaves like $\gamma(s) \sim 1 - \tau_\star^\mu s^\mu$. Plugging this limiting form into the Fourier-Laplace transform of the mobile concentration (4), we find

$$C_m(k,s) = \frac{M_0}{s + \beta\omega\tau_\star^\mu s^\mu - ivk + k^2D}. \tag{72}$$

We call this asymptotic form the fractal model, which coincides with the model analyzed in [45,71,72], as discussed above. We note that even though our model includes the fractal model in the limit $t \gg \tau_\star$, the bifractional models are full models valid for all t on their own. Therefore, we calculate the mobile mass and the moment for all t and not only in the limit $t \to \infty$. The advantage of the ML model is that the trapping PDF (38) is well defined in the limit $t \to 0$.

To find the mobile mass using the fractal model, we set $k = 0$ in $C_m(k,s)$ in Eq. (72) and use the properties of the ML function [see [84], Eq. (3.7.8)], yielding

$$M_m(t) = M_0 E_{1-\mu}(-\beta\omega\tau_\star^\mu t^{(1-\mu)}). \tag{73}$$

For the unnormalized first moment we use the fractal model and the general formula (12) for $\langle x_m(s)\rangle_u$ to find

$$\langle x_m(s)\rangle_u = \frac{v}{[s+\beta\omega(\tau_\star s)^\mu)^2} = \frac{vs^{-2\mu}}{(s^{1-\mu}+\beta\omega\tau_\star^\mu)^2}, \tag{74}$$

which we transform to time domain using [see [90], Eq. (2.5)]

$$\langle x_m(t)\rangle_u = vtE^2_{1-\mu,2}(-\beta\omega\tau_\star^\mu t^{(1-\mu)}). \tag{75}$$

Dividing the unnormalized first moment (75) by the mobile mass (73) normalizes the first moment,

$$\langle x_m(t)\rangle = \frac{vtE^2_{1-\mu,2}(-\beta\omega\tau_\star^\mu t^{(1-\mu)})}{E_{1-\mu}(-\omega\beta\tau_\star^\mu t^{(1-\mu)})}. \tag{76}$$

We plug the fractal model with $\gamma(s) \sim 1 - (\tau_\star s)^\mu$ into the general relation (16) between $\langle x_m^n\rangle_u$ and $\langle x_{im}^n\rangle_u$ for $n = 1$, obtaining

$$\langle x_{im}\rangle_u = \omega\beta v\frac{1}{\{s+\beta\omega[1-\gamma(s)]\}^2}\frac{1-\gamma(s)}{s} = \omega\beta v\frac{\tau_\star^\mu s^{\mu-1}}{(s+\beta\omega\tau_\star^\mu s^\mu)^2}. \tag{77}$$

In the time domain we find, using (77) and Eq. (2.5) in [90], that

$$\langle x_{im}\rangle_u = \omega\beta\tau_\star^\mu t^{2-\mu}E^2_{1-\mu,3-\mu}(-\beta\omega\tau_\star^\mu t^{1-\mu}). \tag{78}$$

Dividing by the immobile fraction mass $M_{im}(t)/M_0 = 1 - M_m(t)/M_0$ yields the normalized first moment

$$\langle x_{im}\rangle = \frac{\omega\beta\tau_\star^\mu t^{2-\mu}E^2_{1-\mu,3-\mu}(-\beta\omega\tau_\star^\mu t^{1-\mu})}{1-E_{1-\mu}(-\beta\omega\tau_\star^\mu t^{(1-\mu)})}. \tag{79}$$

Consider next the unnormalized second moment obtained via the second derivative of $C_m(k,s)$ in Eq. (72),

$$\langle x_m^2(s)\rangle_u = \frac{2D}{(s+\beta\omega\tau_\star^\mu s^\mu)^2} + \frac{2v^2}{(s+\beta\omega\tau_\star^\mu s^\mu)^3} = \frac{2Ds^{-2\mu}}{(s^{1-\mu}+\beta\omega\tau_\star^\mu)^2} + \frac{2v^2s^{-3\mu}}{(s^{1-\mu}+\beta\omega\tau_\star^\mu)^3}, \tag{80}$$

which we transform back to the time domain using Eq. (2.5) in [90],

$$\langle x_m^2(t)\rangle_u = 2Dt E^2_{1-\mu,2}(-\beta\omega\tau_\star^\mu t^{(1-\mu)}) + 2t^2v^2E^3_{1-\mu,3}(-\beta\omega\tau_\star^\mu t^{(1-\mu)}). \quad (81)$$

With the mobile mass (73) we normalize (81) to

$$\langle x_m^2(t)\rangle = 2Dt\frac{E^2_{1-\mu,2}(-\beta\omega\tau_\star^\mu t^{(1-\mu)})}{E_{1-\mu}(-\beta\omega\tau_\star^\mu t^{(1-\mu)})} + 2t^2v^2\frac{E^3_{1-\mu,3}(-\beta\omega\tau_\star^\mu t^{(1-\mu)})}{E_{1-\mu}(-\beta\omega\tau_\star^\mu t^{(1-\mu)})}. \quad (82)$$

We find the second central moment of the fractal model by using relations (76) and (82),

$$\langle[x_m(t)-\langle x_m(t)\rangle]^2\rangle = 2Dt\frac{E^2_{1-\mu,2}(-\beta\omega\tau_\star^\mu t^{(1-\mu)})}{E_{1-\mu}(-\beta\omega\tau_\star^\mu t^{(1-\mu)})} + 2v^2t^2\frac{E^3_{1-\mu,3}(-\beta\omega\tau_\star^\mu t^{(1-\mu)})}{E_{1-\mu}(-\beta\omega\tau_\star^\mu t^{(1-\mu)})} - v^2t^2\left(\frac{E^2_{1-\mu,2}(-\beta\omega\tau_\star^\mu t^{(1-\mu)})}{E_{1-\mu}(-\beta\omega\tau_\star^\mu t^{(1-\mu)})}\right)^2. \quad (83)$$

We note that the asymptotics of the moments presented in this section can be obtained by rewriting the three-parametric ML functions in terms of two-parametric ML functions with Eq. (2.4) in [90] and approximating them up to second order with Eq. (6.11) in [91]. These limits match our results for the EMIM ML model in Sec. III B in Eqs. (42), (45), and (50) and what has been reported previously [46].

V. COMPARISON TO EXPERIMENTS

We apply our model to two different experimental data sets that we discuss in detail. The study reported in [22] probes fluorescent dye in an alpine karst aquifer in the Hochifen-Gottesacker area (Austria). The dye was injected into actively sinking surface water and measured at two karst springs up to 7400 m away [22]. We show the resulting BTC of the data set IP Gb (2) in Fig. 5. It was measured 3500 m downstream from the injection point and was previously reported in [22,92]. Our aim is to obtain the moments of the mobile concentration from this BTC, because BTCs are commonly measured while moments provide important additional information on the transport dynamics [22,27,31,54,69].

One crucial idea of our model is the division into mobile and immobile particles. However, the tracers are not detected while moving through the karst aquifer and hence we cannot directly compare our predicted mobile mass decay to experiments that only measure BTCs. Therefore, we consider a second experiment where the tracer concentration profile is measured. This experiment is the first macrodispersion experiment (MADE-1) [20,43]. The authors of this study realized a 48-h pulse injection of bromide into a heterogeneous aquifer near Columbus, Mississippi (USA). A network of multilevel sampling wells covering around 300 m along the flow direction with approximately 6000 sampling points allowed the observation of the plume profile at eight snapshots up to 594 d after injection. Using linear interpolation between sampling points, the authors obtained the total measured mass by integrating over all three spatial dimensions. The total recovered mass exceeded the initial input mass, which the authors explained by a "spurious hydraulic connection among [the sampling stations]" or higher concentrations in regions with higher hydraulic conductivity and subsequent inaccurate linear interpolation [20]. Nevertheless, a power-law tail was clearly observed in the decay of recovered mass, as demonstrated in [45]. In addition to the mobile mass, the authors obtained the moments of the tracer distribution in the MADE-1 [20]. Notably, the plume consisted of a virtually stationary distribution with a slowly decaying shoulder [20].

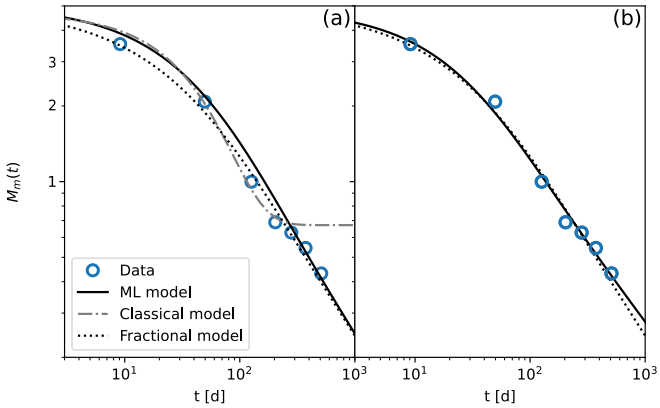

FIG. 3. Fraction of measured mass in the MADE-1. Data points are taken from [45], extracting the data from the PDF paper file. (a) The fractal MIM is fitted to the data; the parameters are $\beta_s = 0.08\ \mathrm{d}^{-0.67}$ and $\mu = 0.33$ with an initial mobile mass of 5, as obtained in [45]. For the ML model (38) we choose $\mu = 0.33$ and $\beta\omega\tau_\star^\mu = 0.08\ \mathrm{d}^{\mu-1}$ such that both the ML and fractal models yield the same long-time asymptotic behaviors. The asymptote does not depend on the ratio $\beta\omega/\tau_\star^\mu$, for which we choose 1/10, 1/5, and 10 from top to bottom. This ratio affects the short-time behavior $\simeq\exp(-\omega\beta t)$. Small values of $\tau_\star$ lead to an early asymptotic behavior and hence a match with the fractal model appears sooner. (b) The exponential model, ML model, and fractal MIM are fitted individually to the data. The asymptotic power law of the ML EMIM has a different exponent of $\mu - 1 = 0.42 - 1 = -0.58$ compared to the fractal model with $\mu - 1 = 0.33 - 1 = -0.67$. The exponential model has the parameters $\beta = 6$, $M_0 = 4.7$, and $\omega = 0.003\ \mathrm{d}^{-1}$, as obtained in [45]. The associated parameters of the remaining models are listed in Table II. Note that "d" represents "day" in SI units.

A. Mobile mass

Figure 3 shows the measured mobile mass decay of the MADE-1 [20] as circles. In Fig. 3(a) we show the best fit of the fractal MIM from [45] (see Sec. IV) along with our ML model. For the latter we do not fit the data but choose the model parameters such that the ML model has the same asymptotic long-time behavior as the fractal model. This is achieved for the parameters $\mu = 0.33$, $\beta\omega\tau_\star^\mu = 0.08\ \mathrm{days}^{\mu-1}$, where in SI units "d" stands for "days", and $M_0 = 5$ for the mobile mass. For the ML model we show the numerical Laplace inversion of the mobile mass in Laplace space (6) using γ_{ML}. At short times all models are dominated by the

TABLE II. Fit parameters and coefficient of determination of fits to $M_m(t)$ from Figs. 3(b) and 4. The parameters β and ω only appear as a product in the mobile concentration and hence cannot be determined separately.

Model	M_0	μ	$\beta\omega$ (d^{-1})	$\tau_\star$ (d)	τ_t (d)	ω_1 (d^{-1})	ω_2 (d^{-1})	b	R^2
ML	4.833	0.417	0.060	9.549					0.992
truncated	4.726	0.226	0.913	0.934	11530				0.994
ML+exp	4.2	0.104	0.0227	25.18		0.0052		0.56	0.998
exp+exp	3.78		0.01983			0.00182	5713	0.61	0.989

identical initial value M_0; hence the ML and fractal models differ only at intermediate timescales of around 50 d. Note that as long as the product $\beta\omega\tau_\star^\mu$ remains constant, the same long-time limit is reached. Therefore, we can choose different ratios $\beta\omega/\tau_\star^\mu$. From top to bottom we use in Fig. 3 the values 1/10, 1/5, and 10. A small ratio will decrease the initial decay $\simeq\exp(-\beta\omega t)$, while a large ratio corresponding to small $\tau_\star$ leads to earlier appearance of the asymptotic behavior, and for the ratio 10, the ML model coincides with the fractal model.

In Fig. 3(b) we show a fit with our model (27) with an exponential trapping time distribution with $\beta = 6$, $M_0 = 4.7$, and $\omega = 0.003\,108\,11$ d^{-1}. These parameters correspond to a fit to the data shown in [45], where a model matching (24) was used. The fit does not describe the data well, because it reaches the steady-state value (27), in contrast to the continued decay shown by the data. In addition, we show fits of both the fractal and ML models to the MADE-1 data. Both models describe the data well, as demonstrated by the coefficient of determination $R^2 = 0.992$ (we calculate all coefficients of determination using the PYTHON module SCIKIT LEARN [93]). In Table II we show the fit parameters, observing no significant difference in goodness of fit between the ML and fractal models. We note, however, that μ differs: It is 0.33 for the fractal model and 0.42 for the ML model. This observation demonstrates that the fully quantitative behavior of the seemingly very similar models is indeed notably different.

Figure 4 shows fits using our extended models from Sec. III D to the MADE-1 data [20,45]; see Table II for the fit parameters. First we consider the composite model with two exponential terms $\gamma(\tau) = b\omega_1\exp(-\omega_1\tau) + (1-b)\omega_2\exp(-\omega_2\tau)$ with $0 < b < 1$. The result is shown by the dotted line, which quantitatively behaves quite similarly to the exponential model. It approximates all but the last data point well with a coefficient of determination of $R^2 = 0.988$, which is notably worse than all models containing power-law waiting times (see Table II). This indicates the necessity of including long-tailed trapping time PDFs for these data. Of course, adding additional exponentials would improve the fit, however, at the cost of a larger number of fit parameters.

The second composite form that we consider reads, in Laplace space,

$$\gamma(s) = \frac{b}{1+(\tau_\star s)^\mu} + (1-b)\frac{\omega_1}{\omega_1+s} \tag{84}$$

and corresponds to the combination of an exponential and an ML trapping time PDF. In Fig. 4 the orange dash-dotted line shows the best fit using this model, with a coefficient of determination of $R^2 = 0.998$. In fact, this is the only model considered here capable of reproducing the apparent shoulder in the data around 200 d. Concurrently, the long-time behavior exhibits a scaling exponent μ that is significantly different from the pure ML model. We highlight that both the truncated ML model (55) with $R^2 = 0.993$ and the combination of the ML and exponential model (84) with $R^2 = 0.998$ fit the data better than the ML model alone ($R^2 = 0.992$). This indicates that the data indeed encode finite-size effects needing a tempering of the power-law tail of the trapping time PDF. However, we stress that we fit to seven data points only and the extended models have more parameters than the ML or exponential model. Therefore, the extended models might be subject to overfitting. Improved data will be needed to be more accurate in this interpretation.

B. Breakthrough curves

In Fig. 5 we show the BTC of the IP Gb (2) experiment, in which fluorescent dye travels in the underground aquifer in the Schwarzwasser valley [22]. All fit parameters are listed in Table III. A fit using the ML trapping time PDF describes the data well with $R^2 = 0.990$. The fractal model describes the data equally well with the same $R^2 = 0.990$. Its peak is slightly higher than that of the ML model. The classical model fails to describe the power-law decay at long times and hence yields the notably worse value $R^2 = 0.940$, with

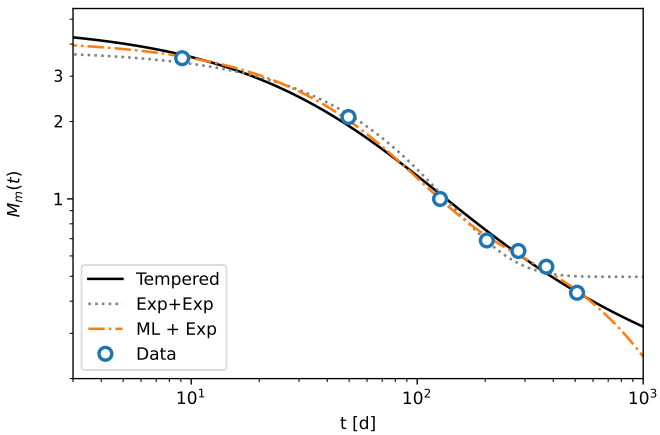

FIG. 4. Fitted extended models. The tempered ML model $\gamma^*_{\rm ML}(s) = [1+(\tau_\star/\tau_t)^\mu]/[1+(\tau_\star s+\tau_\star/\tau_t)^\mu]$ (solid line) and two combinations of γ are fitted to the experimental mobile mass decay of the MADE-1 [20]. At around 900 d, the deviation from the power-law trend is visible in the tempered model. The combination of two exponential functions (dotted line) behaves quite similarly to the pure exponential model in Fig. 3. Combining the ML and exponential models yields the orange dash-dotted line. It is the only model considered capable of describing the shoulder of the data at around 300 d. The fit parameters are given in Table II.

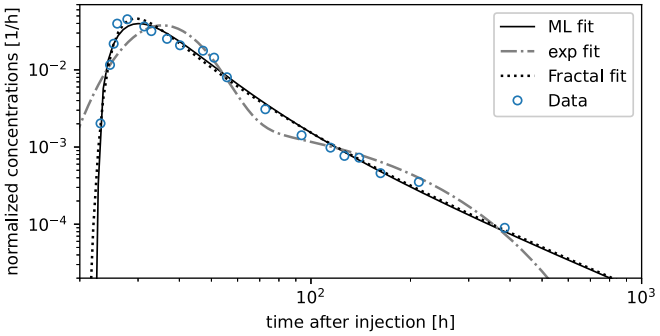

FIG. 5. Fits to the BTC for fluorescent dye measured 3500 m downstream from the injection point in the Schwarzwasser experiment [22,92]. The solid line shows a fit using the ML model with $R^2 = 0.990$ and the dashed line a fit using the fractal model with $R^2 = 0.990$. Both differ mainly in the peak height. An exponential trapping time PDF yields a significantly worse fit ($R^2 = 0.940$) with an additional shoulder and an exponential decay instead of the power-law decay at long times. [Data were taken from [22], IP Gb (2).] The fit parameters are listed in Table III.

an unlikely high fit value for the diffusion coefficient, $D_{\text{exp}} = 9527\ \text{m}^2/\text{h}$, and a considerably lower $v_{\text{exp}} = 94.9\ \text{m/h}$. In this model, the tracers diffuse very fast while the advection is slow. This way, the exponential fit compensates for the lack of the power-law decay. Note also the exponential decay in the fit of the exponential model and the fact that it completely misses the short-time behavior. We conclude that power-law tails introducing a wide range of timescales appear necessary for a proper description of the experimental data. We use the parameters from the fits to the BTC for the remainder of this work.

C. Concentration profile

Next we focus on the spatial distribution of the solute, i.e., the plume profiles. In Fig. 6 we show the concentrations corresponding to the BTC fits in Fig. 5. We logarithmically present the Laplace inversion of the mobile concentration (18) in the top row for the ML model (solid line), the fractal model (dotted line), and the exponential model (dash-dotted line). The left column shows the short-time behavior 1 min after injection. The ML and fractal models show a comparatively narrow bell-shaped behavior, while the exponential model already exhibits a considerable spread due to its high value of D. At intermediate times of 30 h (middle column) all mobile concentrations are increasingly skewed to the right and

TABLE III. Fit parameters and coefficients of determination for the BTCs shown in Fig. 5. The parameters β and ω only appear as a product in the mobile concentration of the ML and fractal model and hence cannot be determined separately.

Model	M_0	μ	$\beta\omega$ (h^{-1})	ω (h^{-1})	$\tau_\star$ (h)	v (m/h)	D (m^2/h)	R^2
ML	155.7	0.737	0.406		0.922	151.4	35.2	0.990
limit	242.8	0.771	0.841		1.00	232.9	21.8	0.990
exp	96.3		0.006	0.011		94.9	9527.0	0.940

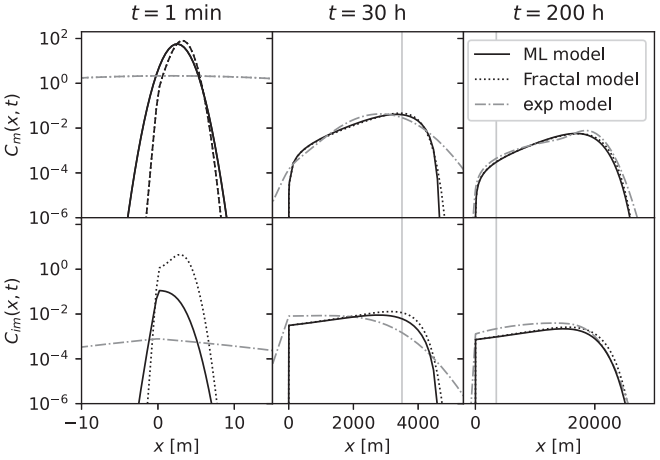

FIG. 6. Logarithmic representation of the concentration profiles of the mobile and immobile particles 1 min, 30 h, and 200 h after injection from the left to the right panels, respectively. Note the different ranges of the horizontal axes for each delay time. At short times all models yield a Gaussian mobile distribution, which is increasingly skewed at later times. The diffusion coefficient $D_{\text{exp}} = 9527\ \text{m}^2/\text{h}$ of the exponential model is exceptionally high compared to that of the ML model ($D_{\text{ML}} = 35.2\ \text{m}^2/\text{h}$) and of the fractal model ($D_{\text{limit}} = 21.8\ \text{m}^2/\text{h}$). Thus the concentration of the exponential model has spread significantly further than the other models at shorter times. The immobile particle fraction has a non-Gaussian distribution at all times and has cusps at $x = 0$, which are typical transport features for systems with diverging waiting times [14,35,71]. The parameters of all models correspond to the fit to the BTC in Fig. 5. The BTC was measured at 3500 m, as marked by the vertical line. See Table III for fit values.

are significantly non-Gaussian (note the different ranges of the horizontal axes for different t). The vertical line denotes the position at which the experimental BTC was measured (3500 m downstream from the injection point). Quick decays to zero concentration around 0 and 4000 m characterize the skewed limit and ML model concentrations. At 200 h, the difference between the three models is quite small. At the measurement position, the limit and ML model are particularly similar.

The immobile concentrations in the bottom row of Fig. 6 are pronouncedly non-Gaussian at all times. We obtain them by taking a numerical Laplace inversion of the mobile concentration (18) plugged into the general relation (5) between the mobile and immobile concentration. At $t = 1$ min the fractal model's immobile concentration is one order of magnitude higher than that of the ML model. In addition, the peak of the ML model is close to $x = 0$ m, while the peak of the fractal model is around $x = 5$ m. At 30 h the ML and fractal models are very similar, have a sharp rise from zero to approximately 10^{-3} at 0 m, and show a peak around 3000 m. In contrast, the exponential model has its peak close to 0 m and falls off monotonically in both directions. At 200 h the ML and fractal models almost coincide and have qualitatively the same shape as for 30 h, although they have spread up to 22 km. Notably, the exponential model has a similar concentration. In the next section we characterize these concentrations further in terms of their first and second moments.

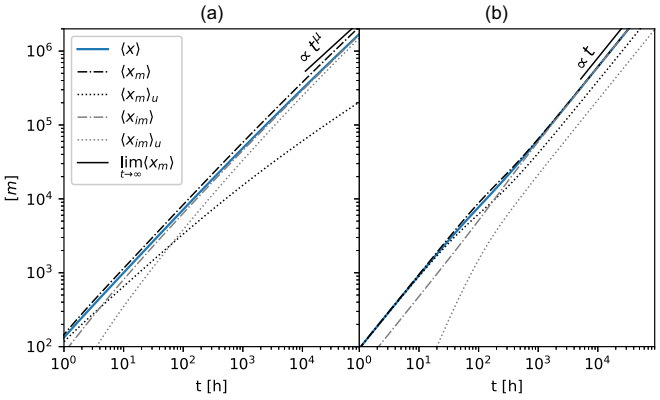

FIG. 7. Comparison of the normalized ($\langle x_{m,im} \rangle$), unnormalized ($\langle x_{m,im} \rangle_u$), and total ($\langle x \rangle$) first moments for the mobile and immobile tracers on a double-logarithmic scale using (a) the ML model and (b) the exponential model. In both panels, both $\langle x_m \rangle_u$ and $\langle x_m \rangle$ are a good approximation for $\langle x \rangle$ at short times, due to the high mobile fraction. The same holds for long times for the immobile moment. In the ML model, the first moment of the mobile particles has the same power-law behavior $\simeq t^{\mu}$ as the immobile tracers but with a larger coefficient. The black solid line shows the asymptote (45) of $\langle x_m \rangle$ as a guide to the eye. The parameters correspond to the fit to the BTC in Fig. 5 as listed in Table III.

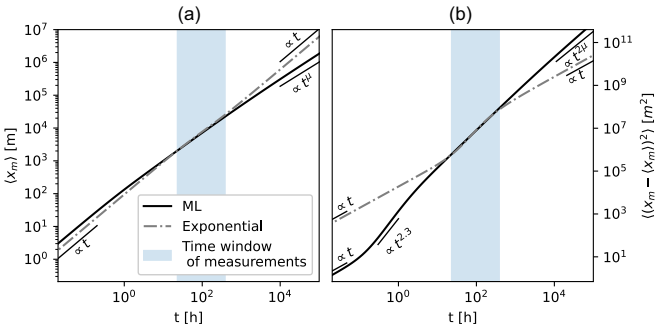

FIG. 8. First ($\langle x_m \rangle$) and second [$\langle (x_m - \langle x_m \rangle)^2 \rangle$] central moments. In (a) we show the first mobile moment using the exponential and ML model (see Fig. 7 for details). In (b) the second central moment of the ML and exponential models scales like $2Dt$ at short times. The exponential model is linear in the long-time limit as well. The ML model grows $\simeq t^{2\mu}$ for $t > 10$ h. The parameters of both models in both panels are taken from the fit to the BTC in Fig. 5 and are listed in Table III. In the shaded regions corresponding to the time window in which the data of the fitted BTCs were taken, the exponential model displays apparent anomalous diffusion and almost coincides with the power-law from the ML model.

D. Moments

We show the first moment $\langle x \rangle$ in Fig. 7 with parameters corresponding to the fit of our model to the BTC in Fig. 5. In addition to $\langle x \rangle$ we show the first moment of the mobile and immobile tracers $\langle x_m \rangle$ and $\langle x_{im} \rangle$, respectively. For the exponential model we use the analytic expressions (28) for $\langle x_m \rangle_u$ and (30) for $\langle x_m \rangle$. All remaining first moments are obtained through Laplace inversion of the general expressions (12) for $\langle x_m \rangle_u$ and (16) for $\langle x_{im} \rangle_u$. Subsequent normalization with the mobile mass (40) yields $\langle x_m \rangle$ and $\langle x_{im} \rangle$ for the ML model.

The first moment $\langle x \rangle$ of the total mass in Fig. 7 demonstrates a crossover from linear to power-law ($\simeq t^{\mu}$) scaling in time when using the ML model. At short times it matches $\langle x_m \rangle$ and $\langle x_m \rangle_u$, while coinciding with $\langle x_{im} \rangle$ and $\langle x_m \rangle_u$ at long times, as expected by the immobilization of all tracers in the long-time limit. The moments $\langle x_m \rangle$ and $\langle x_{im} \rangle$ have the same long-time power-law behavior, albeit with different coefficients. The black solid line in Fig. 7(a) shows the long-time limit of $\langle x_m \rangle$ using the ML model as given by the expression (45). In contrast, the center of mass of the mobile plume of the ML model is ahead at all times after injection. In Fig. 11 the described behavior is easier to discern with a significantly lower $\mu = 0.33$. We use the parameters of the fit to the mobile mass in [45] of Fig. 3 along with $v = 0.8$ m/d and $D = 4\text{m}^2/\text{d}$. The advection speed v was measured in the experiment and D is our estimate. In the time interval in which the BTC data were collected, the first mobile moments almost coincide and grow nonlinearly $\simeq t^{\mu}$, including the exponential model, as shown in Fig. 8.

In Fig. 9 we show the second moments corresponding to the BTC fits from Fig. 5. We obtain the moments through Laplace inversion of the general expressions (14) for $\langle x_m^2(s) \rangle_u$ and (16) for $\langle x_{im}^2 \rangle_u$ after normalization with $M_m(t)$ or $M_{im} = M_0 - M_m$ [obtained from the general expression (6) for $M_m(s)$]. The second moment of the total concentration obtained from the general expression (17) for $\langle x^n \rangle$ agrees with $\langle x_m^2 \rangle$ for both the ML and exponential order models at short times as almost all tracers are mobile at this time. In contrast to the ML model, the first-order model shows a crossover from linear to quadratic behavior. Around 1000 h, $\langle x^2 \rangle$ and $\langle x_{im}^2 \rangle$ coincide and grow proportionally to $t^{2\mu}$. The second mobile moment has the same power-law growth, albeit with a higher prefactor, as demonstrated by the long-time limit (50) of $\langle x_m^2 \rangle$

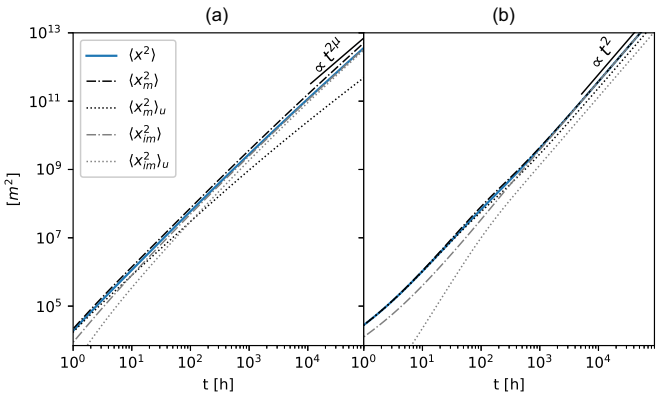

FIG. 9. Comparison of the normalized ($\langle x_{m,im}^2 \rangle$), unnormalized ($\langle x_{m,im}^2 \rangle_u$), and total ($\langle x^2 \rangle$) second moments for the mobile and immobile tracers on a double-logarithmic scale. All models yield $\langle x^2(t) \rangle = \langle x^2(t) \rangle_u \approx 2Dt$ at short times. (a) At long times the ML model show anomalous diffusion $\langle x^2 \rangle \simeq t^{2\mu}$, i.e., superdiffusion for $1/2 < \mu < 1$. (b) The exponential trapping time PDF leads to the long-time growth $v^2t^2/(1+\beta)^3$ and $v^2t^2/(1+\beta)^2$ of $\langle x_m^2 \rangle_u$ and $\langle x_m^2 \rangle$, respectively. The black solid line shows the asymptote (50) of $\langle x_m^2 \rangle$ as a guide to the eye. The parameters are the same as in Fig. 3(a).

shown as a black solid line. In the exponential model, all normalized second moments grow quadratically and overlap around 1000 d, as expected by the equivalence of C_m and C_{im} [Eq. (26)] at long times. Figure 8 shows the first and second central moments of the mobile concentration, the latter of which is obtained via $\langle(x_m - \langle x_m\rangle)^2\rangle = \langle x_m^2\rangle - \langle x_m\rangle^2$. Note that only the analysis of normalized second central moments is meaningful; therefore, we do not explicitly study the second central moment of the unnormalized moments. At short times, both the ML (solid line) and exponential (dash-dotted line) models grow linearly. The prefactor D of the latter is two orders of magnitude larger and the linear regime lasts until around 10 h. The ML model yields linear growth up to 6 min and transitions to the power law $t^{2\mu}$ after a transient growth proportional to $t^{2.3}$ around 30 min. In the range from 20 to 300 h we fitted our models to the BTCs as shown in Fig. 5. In this range, which we highlight by the shaded areas in Fig. 8 (and only in this range), the first and second central moments of the two models almost coincide. Hence, the exponential model can show transient anomalous diffusion. This is a remarkable result. Outside this time window at longer times the moments demonstrate distinct differences. The exponential model shows normal diffusion with $\langle(x_m - \langle x_m\rangle)^2\rangle \simeq t$, while the mobile particles in the ML model spread faster with $\langle(x_m - \langle x_m\rangle)^2\rangle \simeq t^{2\mu}$.

Here we analyzed anomalous diffusion using the first and second moments, while higher moments can reveal non-Gaussianity properties of the concentration profile. In Appendix D we calculate the skewness and kurtosis. These clearly show that after short times both the mobile and immobile concentrations are non-Gaussian when using the ML model. For $t \to \infty$, we find that the skewness and kurtosis only depend on μ. Notably, both appear to be discontinuous at $\mu = 1$ and jump to their respective Gaussian values.

VI. CONCLUSION

We introduced and discussed the extended mobile-immobile model for tracer motion in which the residence time in the immobile domain is drawn from a general trapping time PDF $\gamma(t)$. The mobile times were chosen to always follow an exponential distribution. A system with an exponential trapping time PDF could then be rewritten in terms of a classical first-order mass transfer model [26]. We considered the initial condition when all particles are mobile after a pulse injection. This leads to a Gaussian mobile plume at short times for any $\gamma(t)$. At intermediate times particles in the mobile phase are trapped in the immobile zone following an exponential trapping time PDF which renders the mobile concentration non-Gaussian and the moments grow nonlinearly. The second central moment exhibits an apparent anomalous diffusion in this time regime. In the long-time limit the mobile and immobile concentrations coincide and we recover normal diffusion with a rescaled time $t/(1 + \beta\langle\tau\rangle\omega)$, where β denotes the ratio of immobile to mobile volume, $\langle\tau\rangle$ represents the average immobilization time, and ω in time stands for the mass transfer coefficient.

When using a scale-free trapping time PDF with power-law tail $\simeq t^{-\mu-1}$ with $0 < \mu < 1$ and diverging mean waiting time, such as the ML PDF considered here, all tracers immobilize eventually with a long-time power-law decay $\simeq t^{\mu-1}$ of the mobile mass. Our model with a ML PDF contains the fractal MIM from [45] and the bifractional diffusion model from [71,72,89] for specific choices of the scaling exponents as special cases. We found analytical results up to the second moment in this special case that hold for all times. Our ML model showed good fit results to the mobile mass decay of the MADE-1 [20]. In addition, we considered two extensions of the immobilization time PDF $\gamma(\tau)$. First we introduced an exponential tempering to analyze truncation effects. Second we considered a weighted sum of an ML PDF and an exponential PDF. Both modifications yielded even better fit results than the ML model alone. While these extended forms involve additional model parameters, their better fit indicates that cutoffs in the power-law trapping time density reflect better the physical situation, i.e., the system appears to show finite-size effects, similar to those obtained in trapping time PDFs in the conductivity study [31].

The ML model yielded a good fit to the BTC ($R^2 = 0.990$) of tracers in karst aquifers from [22]. This allowed us to obtain model parameters including the advection velocity and dispersion coefficient in the mobile zone. Subsequently, we calculated the moments of the mobile distribution and accounted for time-dependent normalizations. We found temporally nonlinear mass transport $\langle x\rangle \simeq t^{\mu}$ and anomalous diffusion $\langle(x - \langle x\rangle)^2\rangle \simeq t^{2\mu}$ in the long-time limit. Concurrently, the concentration crossed over to a non-Gaussian immobile concentration. Mobile tracers led the immobile tracers in this long-time limit. We characterized the non-Gaussianity using the skewness and kurtosis, of which the long-time limit only depends on μ, as shown in Appendix D.

Notably, a fit to the BTC with an exponential model matched the data quite reasonably ($R^2 = 0.940$) but yielded an unlikely high diffusion constant. Nevertheless, the mobile concentration profiles appeared reasonably similar for $t = 30$ h and almost matched for $t = 200$ h. The exponential model showed transient anomalous diffusion in this time window, and the second central moment almost coincided with the ML model. It is remarkable that the exponential and ML models have a fundamentally different long-time behavior but yield very similar first, second, and second central moments in the intermediate time window, where the BTC measurements were taken. In fact, our analysis demonstrated that from experimental data it is rather tricky to distinguish even fundamentally different models based on transport moments. The mobile mass, BTC, and concentration profile are much better suited for this purpose. However, once fitted to the data, the moments demonstrate the massively different transport efficiency at long times. Such knowledge is of high relevance, e.g., to study the environmental impact of chemicals released into rivers or aquifers. The existence of long retention times may be underestimated by fits to exponential models and thus neglect potentially dangerous leakage of chemicals at much longer times.

The situation is quite different in other systems in which more extensive data are available, such as from simulations or single-particle-trapping experiments in live biological cells

or complex liquids. In such systems the moments can be efficiently extracted and compared to different models. There, particles can undergo diffusion with intermittent immobilization as well. An example could be proteins diffusing in the bulk cytoplasm of a live cell with intermittent binding to membrane receptors. In fact, three-dimensional trajectories of mRNA particles in yeast cells have been observed to switch between diffusive, directed, and confined motion as well as becoming stationary [94], similar to amoeboid motion on surfaces [95]. Single-molecule tracking of signaling proteins reveals intermittent dynamics during which proteins effectively immobilize on activation [96]. Membrane proteins and proteins in the cell nucleus have been observed to split into mobile and immobile populations [63,97,98]. We mention molecular dynamics simulations of drug molecules in a water layer confined in a silica slit unveiling intermittent immobilization due to surface adsorption with power-law-distributed trapping times [99]. Similar waiting time distributions are observed in the short-time motion of lipid granules in live yeast cells [100]. In fact, for systems with power-law-distributed immobilization times or diffusion with strongly position-dependent diffusivity populations, splitting is a salient feature [75,76,101].

The MIM can also be thought of as a special case of switching diffusion, when a particle intermittently undergoes different modes of transport within a single trajectory [102–104]. When adding an advection-diffusion operator to the immobile concentration of the EMIM a switching diffusion process could be obtained. In [102,103] a single particle switches between states with different diffusivities with fixed rates. If the observation time is small compared to the mean residence time, transport anomalies arise. Examples for switching diffusion include quantum dot tracers in the cytoplasm of mammalian cells which switch between different mobilities [105]. Molecular dynamics simulations show that conformal changes of proteins induce fluctuations of the protein diffusivity [106]. A simple model of particles that can aggregate and separate shows similar behavior [107]. Polymers change diffusivity during (de)polymerization due to varying chain lengths leading to transient non-Gaussian displacement PDFs [104]. Switching behavior is also seen in potassium channels and nonintegrin receptors in living cell membranes [108,109] as well as for lipid motion in molecular dynamics simulations of protein-crowded bilayer membranes [110]. Similar population splitting is observed in the passive motion of tracers in mucin gels [111,112] or acetylcholine receptors in live cell membrane [113]. Population splitting into fractions with different diffusivities was also observed for individually labeled lipids in the phospholipid membrane and of H-Ras proteins at the plasma membrane [114,115]. Moreover, G proteins have been observed to switch between states with different diffusivities due to conformational changes and increased immobilization after interaction [116]. These cases of molecular transport can represent scenarios in which our EMIM or its extensions can provide relevant insight into population splitting between mobile and immobile particle fractions and their respective transport dynamics. Moreover, the breakthrough curves discussed here can be used to deduce the first-passage dynamics to some reaction center.

Our model is a starting point to describe molecular reactions of anomalously diffusing tracers, such as reactions occurring in mobile and immobile zones in rivers or reactions of molecules or tracers in biological cells. Recently, reaction-subdiffusion systems have been analyzed using the Fokker-Planck-Kolmogorov equation [117]. With our model it is possible to model reactions that only occur when the particles immobilize and to find explicit equations for the reaction products. We believe that the EMIM presented here provides a flexible and unified description for mobile-immobile transport.

ACKNOWLEDGMENTS

We acknowledge funding from the German Science Foundation (Grant No. DFG ME 1535/12-1). R.M. acknowledges the Foundation for Polish Science (Fundacja na rzecz Nauki Polskiej) for funding within an Alexander von Humboldt Polish Honorary Research Scholarship. A.V.C. acknowledges support from the Polish National Agency for Academic Exchange (NAWA).

APPENDIX A: MOBILE MASS USING THE ML TRAPPING TIME PDF

We calculate the mobile mass (6) for the concrete ML form of the trapping time PDF. In Laplace space we find

$$M_m(s) = \frac{M_0}{s + \omega\beta\left[1 - \frac{1}{1+\tau_\star^\mu s^\mu}\right]} \tag{A1}$$

$$= \frac{M_0(1+\tau_\star^\mu s^\mu)}{s(1+\tau_\star^\mu s^\mu) + \omega\beta\tau_\star^\mu s^\mu} \tag{A2}$$

$$= \frac{M_0(1+\tau_\star^\mu s^\mu + \beta\omega\tau_\star^\mu s^{\mu-1}) - M_0\beta\omega\tau_\star^\mu s^{\mu-1}}{s(1+\tau_\star^\mu s^\mu + \beta\omega\tau_\star^\mu s^{\mu-1})} \tag{A3}$$

$$= \frac{M_0}{s} - M_0\beta\omega\tau_\star^\mu \frac{s^{\mu-2}}{\tau_\star^\mu s^\mu + \beta\omega\tau_\star^\mu s^{\mu-1} + 1}. \tag{A4}$$

Now we use the geometric series for $s^{1-\mu} < \tau_\star^\mu s + \beta\omega\tau_\star^\mu$,

$$\frac{1}{\tau_\star^\mu s^\mu + \beta\omega\tau_\star^\mu s^{\mu-1} + 1}$$

$$= \frac{s^{1-\mu}}{\tau_\star^\mu s + \beta\omega\tau_\star^\mu} \frac{1}{1 + \frac{s^{1-\mu}}{\tau_\star^\mu s + \beta\omega\tau_\star^\mu}} \tag{A5}$$

$$= \frac{s^{1-\mu}}{\tau_\star^\mu s + \beta\omega\tau_\star^\mu} \sum_{k=0}^{\infty} (-1)^k \frac{s^{k(1-\mu)}}{(\tau_\star^\mu s + \beta\omega\tau_\star^\mu)^k} \tag{A6}$$

$$= \sum_{k=0}^{\infty} \frac{(-1)^k}{\tau_\star^{\mu(1+k)}} \frac{s^{k(1-\mu)+(1-\mu)}}{(s+\beta\omega)^{k+1}} \tag{A7}$$

$$= \frac{1}{s\tau_\star^\mu(s+\beta\omega)} + \sum_{k=1}^{\infty} (-1)^k \frac{(-1)^k}{\tau^{\mu(1+k)}} \frac{s^{k(1-\mu)+(1-\mu)}}{(s+\beta\omega)^{k+1}}. \tag{A8}$$

We use the Laplace inversion [Eq. (2.5) in [90]] and (A8) to transform (A4) to the time domain

$$M_m(t) = M_0 - M_0\beta\omega\tau_\star^\mu \Bigg[\frac{1}{\beta\omega\tau_\star^\mu}(1 - e^{-\beta\omega t}) + M_0 e^{-\beta\omega t} \sum_{k=1}^{\infty} (-1)^{k+1} \frac{t^{\mu k+1}}{\tau^{\mu(k+1)}} E^{k+1}_{1,\mu k+2}(-\beta\omega t) \Bigg]$$

$$= M_0 e^{-\beta\omega t} + N_0 \beta\omega t \sum_{k=1}^{\infty} (-1)^{k+1} \left(\frac{t}{\tau}\right)^{\mu k} \times E^{k+1}_{1,\mu k+2}(-\beta\omega t). \tag{A9}$$

According to Gorenflo *et al.* [see [84], Eq. (5.1.54)], $E^{\delta}_{1,\beta}(z) = \frac{1}{\Gamma(\beta)}{}_1F_1(\delta, \beta, z)$ and thus from (A9),

$$M_m(t) = M_0 e^{-\beta\omega t} + M_0\beta\omega t \sum_{k=1}^{\infty} \frac{(-1)^{k+1}}{\Gamma(\mu k + 2)} \left(\frac{t}{\tau_\star}\right)^{\mu k} \times M(k+1, \mu k + 2, -\beta\omega t), \tag{A10}$$

where ${}_1F_1(a, b, z) \equiv M(a, b, z)$ is the Kummer function [84].

APPENDIX B: LONG-TIME CONCENTRATION PROFILE

Consider the fractal model. We approximate $C_m(x, s)$ [Eq. (18)] using $\sqrt{1+z} \sim 1 + z/2$ in the exponential and $\sqrt{1+z} \sim 1$ in the first fraction for $z = 4\phi(s)D/v^2 \ll 1$,

$$C_m(x, s) \overset{s\to 0}{\sim} \frac{e^{vx/2D}}{v} e^{-(v/2D)[1+2\phi(s)D/v^2]|x|} \tag{B1}$$

$$\overset{s\to 0}{\sim} \frac{1}{v} e^{(v/2D)(x-|x|)} e^{-\beta\omega\tau_\star^\mu s^\mu (|x|/v)}, \tag{B2}$$

by using $\phi(s) = s + \beta\omega\tau_\star^\mu s^\mu \approx \beta\omega\tau_\star^\mu s^\mu$ for small s. In [84], Sec. 7.5, we find the Laplace transform pairs

$$\mathscr{L}^{-1}\{e^{-cs^\mu}\} = \frac{c\mu}{t^{\mu+1}} M_\mu(ct^{-\mu}), \tag{B3}$$

$$\mathscr{L}^{-1}\{s^{\mu-1}e^{-cs^\mu}\} = \frac{1}{t^\mu} M_\mu(ct^{-\mu}) \tag{B4}$$

for $c > 0$, with the auxiliary function of Wright type

$$M_\mu(z) = \sum_{n=0}^{\infty} \frac{(-z)^n}{n!\Gamma[-\mu n + (1-\mu)]}. \tag{B5}$$

This yields the long-time limit of the mobile concentration

$$C_m(x, t) \approx \frac{\beta\omega\tau_\star^\mu \mu}{v^2} e^{(v/2D)(x-|x|)} |x| t^{-1-\mu} M_\mu\left(\frac{\beta\omega\tau_\star^\mu}{v}|x|t^{-\mu}\right) \tag{B6}$$

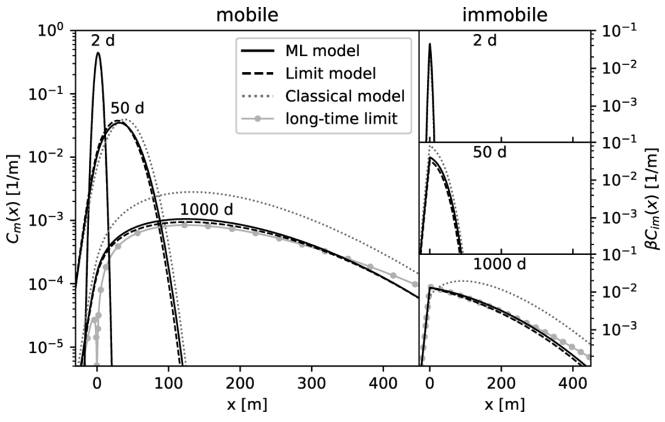

FIG. 10. Concentrations of mobile and immobile particles 2, 50, and 1000 d after injection in the main and right panels, respectively. The parameters of all models correspond to the fit to the mobile mass decay shown in Fig. 3. At short times all models yield a Gaussian mobile distribution, which is increasingly skewed for later times. Immobile particles have a non-Gaussian distribution at all times. Cusps are clearly visible at $x = 0$ and are a typical transport feature for systems with diverging trapping times [14,35]. The long-time behaviors (B6) and (B7) are shown by the gray lines with markers. The root at $x = 0$ for the mobile concentration is an artifact of our approximation (see the text). We use 0.8 m/d and 4 m^2/d for v and D, respectively. The parameters of the ML model can be found in Table II. The parameters for the classical and fractional model correspond to a fit in [45] to the mobile mass decay of the MADE-1, as can be seen in Fig. 3 together with the parameters [45].

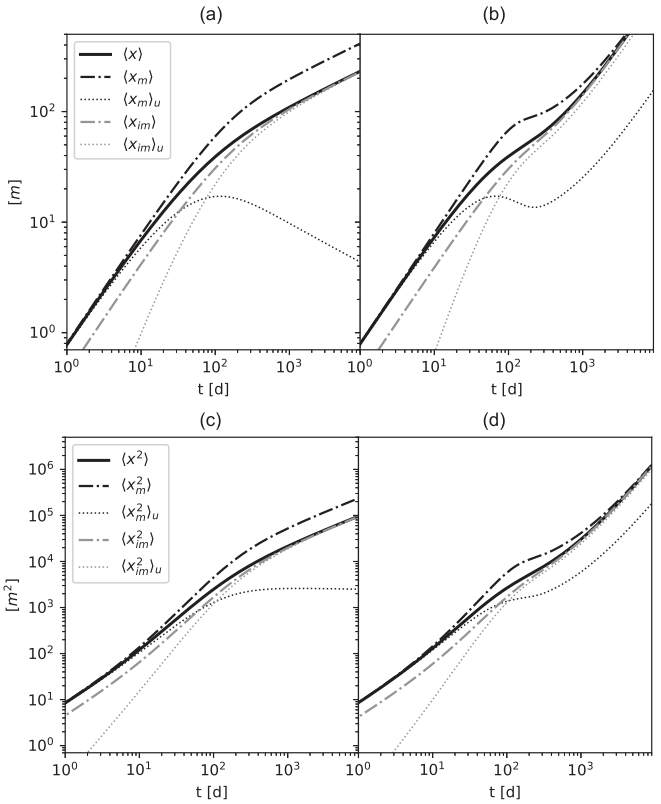

FIG. 11. Comparison of the normalized ($\langle x^n_{m,im} \rangle$), unnormalized ($\langle x_{m,im} \rangle_u$) and total nth-order ($\langle x^n \rangle$) moments, for (a) and (b) $n = 1$ and (c) and (d) $n = 2$ with double-logarithmic scales, using (a) and (c) the ML model and (b) and (d) the exponential model. For both models, both $\langle x_m \rangle_u$ and $\langle x_m \rangle$ are a good approximation for $\langle x \rangle$ for short times, due to the high mobile fraction. The same holds for long times for the immobile moment. In the ML model, the first moment of the mobile particles has the same power-law behavior (proportional to t^μ) as the immobile tracers but with a larger coefficient. The parameters are the same as in Fig. 3(a) and are given in Table II.

and the long-time limit of the immobile concentration using $C_{im}(x,s) = \omega\frac{1-\gamma(s)}{s}C_m(x,s)$ with $\gamma(s) \approx 1 - \tau_\star^\mu s^\mu$,

$$C_{im}(x,t) \approx \frac{\beta\omega\tau_\star^\mu}{v} e^{(v/2D)(x-|x|)} t^{-\mu} M_\mu\left(\frac{\beta\omega\tau_\star^\mu}{v}|x|t^{-\mu}\right). \quad \text{(B7)}$$

In Fig. 10 we show these approximations. Notice that at $t = 1000$ d, these approximations, shown as a gray line with markers, indeed estimate quite well the results obtained from the inverse Laplace inversion. Note also how the factor $|x|$ and finite value of $M_\mu(0) = 1/\Gamma(1-\mu)$ lead to a dip to zero at $x = 0$ for this approximation. This is an artifact of our approximation of $C_m(x,s)$ [Eq. (B2)], as it does not depend on s for $x = 0$.

APPENDIX C: ADDITIONAL PLOTS OF MOMENTS

We show additional plots of the first and second moments in Fig. 11. Figures 11(a) and 11(c) show our model using an ML trapping time PDF and Figs. 11(b) and 11(d) using an exponential trapping time PDF. The former demonstrates a transition from normal Brownian to anomalous behavior.

APPENDIX D: SKEWNESS AND KURTOSIS

Similarly to (14), we calculate the third and fourth unnormalized moments

$$\langle x_m^3(s)\rangle_u = -i\frac{\partial^3}{\partial k^3}\frac{C_m(k,s)}{M_0}\bigg|_{k=0} = \frac{12Dv}{\{s+\beta\omega[1-\gamma(s)]\}^3} + \frac{6v^3}{\{s+\beta\omega[1-\gamma(s)]\}^4},$$

$$\langle x_m^4(s)\rangle_u = \frac{\partial^4}{\partial k^4}\frac{C_m(k,s)}{M_0}\bigg|_{k=0} = \frac{24D^2}{\{s+\beta\omega[1-\gamma(s)]\}^3} + \frac{72Dv^2}{\{s+\beta\omega[1-\gamma(s)]\}^4} + \frac{24v^4}{\{s+\beta\omega[1-\gamma(s)]\}^5}. \quad \text{(D1)}$$

When dividing by the fraction of mobile mass, we can calculate the skewness

$$\tilde{\mu}_{3,m} = \left\langle\left(\frac{x_m - \langle x_m\rangle}{\sqrt{\langle(x_m - \langle x_m\rangle)^2\rangle}}\right)^3\right\rangle \quad \text{(D2)}$$

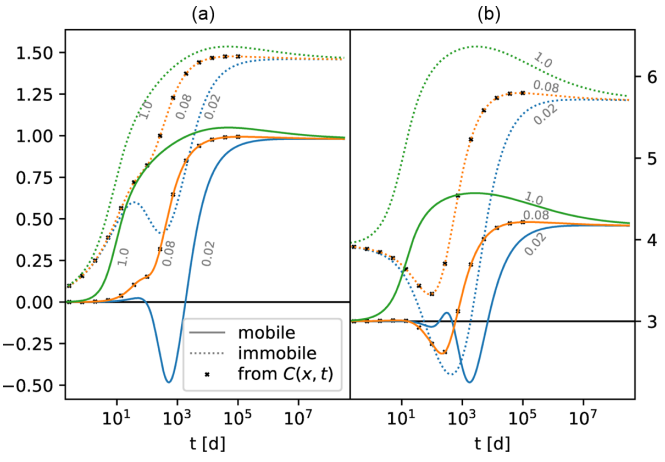

FIG. 12. (a) Skewness and (b) kurtosis for the ML model. Limits are calculated with the derivatives (D1) in Fourier space. Small numbers next to the lines indicate the values of β. Crosses mark the corresponding values for $\beta = 0.08$ obtained from the plume profile (18) after numerical Laplace inversion. The remaining parameters are the same as in Fig. 3(a), i.e., we have $\mu = 0.33$, $\omega = 1$ d^{-1}, and $\tau_\star = 1$ d.

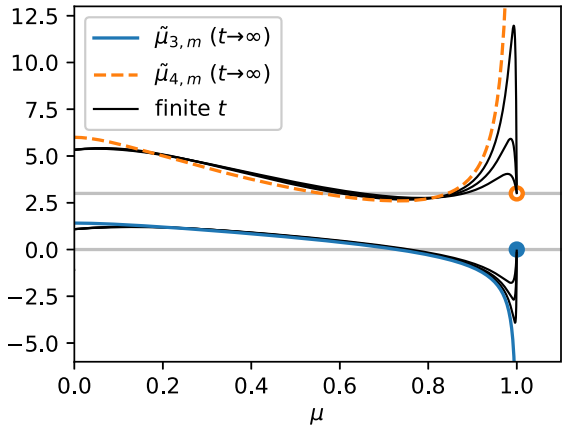

FIG. 13. Long-time limits of the skewness (D2) and kurtosis (D3) that only depend on μ and the sign of v (chosen positive here) for the ML and fractal models. The expressions for $\mu < 1$ diverge for $\mu \to 1$. For $\mu = 1$, we have $\tilde{\mu}_{3,m} = 0$ and $\tilde{\mu}_{4,m} = 1$. Gray lines indicate these values. Black solid lines indicate the kurtosis for finite $t = 500, 200, 100$ from top to bottom. They all reach the Gaussian value of 3 at $\mu = 1$ and are continuous. The skewness for finite $t = 500, 1000, 2000$ shows black solid lines ending at zero for $\mu = 1$. They are continuous as well. Black lines were obtained from the asymptotic expressions of the moments for $\beta = v = D = 1$.

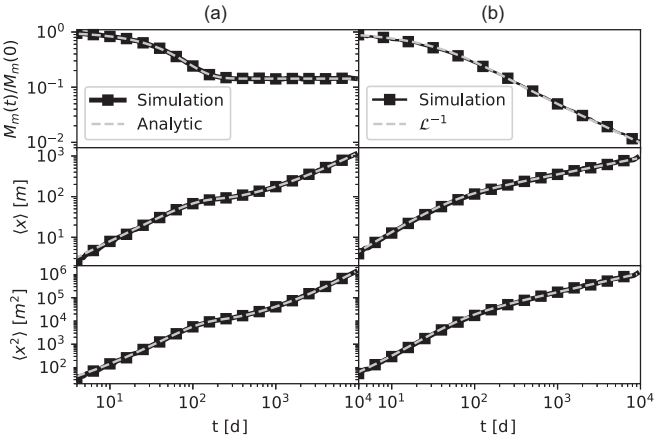

FIG. 14. Validation of our results with particle-tracking simulations. Square symbols denote values obtained from simulations using the method proposed in [66]. (a) For the exponential model we use our analytical results and (b) for the ML model we compare the simulations results to Laplace inversions of (12) and (14). The parameters are the same as in Fig. 3(a).

and kurtosis

$$\tilde{\mu}_{4,m} = \left\langle \left(\frac{x_m - \langle x_m \rangle}{\sqrt{\langle (x_m - \langle x_m \rangle)^2 \rangle}} \right)^4 \right\rangle \tag{D3}$$

of the mobile solutes. Using (5), we obtain the skewness and kurtosis for the immobile plume.

A normal distribution in one dimension has skewness 0 and kurtosis 3. Deviations from these values characterize non-Gaussianity. Figure 12 shows the skewness and kurtosis using the ML model for different values of β for $\omega\tau_\star = 1$. The mobile plume shows no initial skewness, as expected by the short-term Gaussian distribution. Small values of β yield negative skewness for intermediate timescales, i.e., a leading edge of the mobile plume profile. In [45] negative skewness is found for small β as well. We find that the long-time limit of the skewness is independent of β and positive for $\mu \lessapprox 0.73$. In addition, we numerically find positive skewness for intermediate times when decreasing v and leaving all remaining parameters constant for $\mu = 0.33$ and $\beta = 0.01$.

The long-time limit is independent of β and positive for the chosen $\mu = 0.33$. This corresponds to a leading tail of the mobile plume profile. The immobile distribution has positive skewness at all timescales and is nonmonotonic for $\beta = 0.02$. To verify our results, we additionally calculate the skewness and kurtosis from the plume profile (18) for $\beta = 0.08$. The resulting crosses in Fig. 12 show good agreement.

The kurtosis measures how much of a distribution is concentrated in the tails. As Fig. 12 shows, the mobile distribution starts at 3 and has minima at intermediate times below this value for $\beta = 0.02$ and 0.08.

We calculate the long-time limits

$$\left\langle x_m^3 \right\rangle \approx \frac{\frac{12Dvt^{3\mu-1}}{\beta^3\Gamma(3\mu)} + \frac{6v^3t^{4\mu-1}}{\beta^4\Gamma(4\mu)}}{\frac{t^{\mu-1}}{\beta\Gamma(\mu)}} \tag{D4}$$

and

$$\left\langle x_m^4 \right\rangle \approx \frac{\frac{24D^2t^{3\mu-1}}{\beta^3\Gamma(3\mu)} + \frac{72Dv^2t^{4\mu-1}}{\beta^4\Gamma(4\mu)} + \frac{24v^4t^{5\mu-1}}{\beta^5\Gamma(5\mu)}}{\frac{t^{\mu-1}}{\beta\Gamma(\mu)}} \tag{D5}$$

by using the Tauberian theorem. These results match earlier results found in [46]. We plug these into (D2) and (D3). For $\mu = 1$ we find $\tilde{\mu}_3 = 0$ and $\tilde{\mu}_4 = 3$, which match the normal distribution for $\mu = 1$ found in [45]. The long-time limits of the skewness only depend on μ and the sign of v, which we assume to be positive, here

$$\begin{aligned}
\lim_{t\to\infty} \tilde{\mu}_3 = &- \frac{2\sqrt{\frac{\Gamma(3\mu)}{\Gamma(\mu)}}[12\sqrt{\pi}\Gamma(\mu)\Gamma(2\mu)^3\Gamma(4\mu) - 12\sqrt{\pi}\Gamma(2\mu)^4\Gamma(3\mu)]}{[2\Gamma(2\mu)^2 - \Gamma(\mu)\Gamma(3\mu)]^{3/2}\left[4\sqrt{\pi}\Gamma(2\mu)\Gamma(4\mu) - 16^\mu\Gamma(\mu)\Gamma(3\mu)\Gamma\left(2\mu+\frac{1}{2}\right)\right]} \\
&- \frac{2\sqrt{\frac{\Gamma(3\mu)}{\Gamma(\mu)}}\left[16^\mu\Gamma(\mu)^3\Gamma(3\mu)^2\Gamma\left(2\mu+\frac{1}{2}\right) - 4\sqrt{\pi}\Gamma(\mu)^2\Gamma(2\mu)\Gamma(3\mu)\Gamma(4\mu)\right]}{[2\Gamma(2\mu)^2 - \Gamma(\mu)\Gamma(3\mu)]^{3/2}\left[4\sqrt{\pi}\Gamma(2\mu)\Gamma(4\mu) - 16^\mu\Gamma(\mu)\Gamma(3\mu)\Gamma\left(2\mu+\frac{1}{2}\right)\right]} \\
&- \frac{2\sqrt{\frac{\Gamma(3\mu)}{\Gamma(\mu)}}\left\{-3\Gamma(\mu)\Gamma(2\mu)^2\Gamma(3\mu)\left[16^\mu\Gamma(\mu)\Gamma\left(2\mu+\frac{1}{2}\right) - 2\sqrt{\pi}\Gamma(3\mu)\right]\right\}}{[2\Gamma(2\mu)^2 - \Gamma(\mu)\Gamma(3\mu)]^{3/2}\left[4\sqrt{\pi}\Gamma(2\mu)\Gamma(4\mu) - 16^\mu\Gamma(\mu)\Gamma(3\mu)\Gamma\left(2\mu+\frac{1}{2}\right)\right]},
\end{aligned} \tag{D6}$$

while the long-time limit of the kurtosis only depends on μ,

$$\begin{aligned}
\lim_{t\to\infty} \tilde{\mu}_4 = &- \frac{3\Gamma(3\mu)[8\Gamma(\mu)\Gamma(2\mu)^3\Gamma(3\mu)\Gamma(5\mu) - 8\Gamma(2\mu)^4\Gamma(3\mu)\Gamma(4\mu)]}{\Gamma(\mu)[\Gamma(\mu)\Gamma(3\mu) - 2\Gamma(2\mu)^2]^2\Gamma(4\mu)\Gamma(5\mu)} \\
&- \frac{3\Gamma(3\mu)[\Gamma(3\mu)\Gamma(4\mu)\Gamma(5\mu)\Gamma(\mu)^3 + 4\Gamma(2\mu)^2\Gamma(4\mu)\Gamma(5\mu)\Gamma(\mu)^2]}{\Gamma(\mu)[\Gamma(\mu)\Gamma(3\mu) - 2\Gamma(2\mu)^2]^2\Gamma(4\mu)\Gamma(5\mu)}.
\end{aligned} \tag{D7}$$

Figure 13 shows the limiting values. The skewness takes positive values for $\mu < 0.73$, i.e., the mobile plume has a leading tail, and negative values otherwise. The kurtosis is always higher than 3 except for $0.56 < \mu < 0.84$, meaning that for $0.56 < \mu < 0.84$ more mobile particles are within the standard deviation than for a normal distribution and thus effect a pronouncedly non-Gaussian distribution.

We note the apparent discontinuity of the long-time limits of the skewness (D6) and kurtosis (D7), as shown in Fig. 13. Note that we get finite values of the kurtosis for finite t, as evidenced by Fig. 13. A more detailed analysis of this property is beyond the scope of the present work.

APPENDIX E: SIMULATION

We implement a particle-tracking simulation using the space-domain method [66], in which the particle makes a jump Δx drawn from the jump length PDF $\lambda(x)$ in the fixed time Δt [66]. After each jump the particle immobilizes for a duration drawn from $\psi(t)$ with probability $1 - \exp(-\omega\beta\Delta t)$. For a waiting time PDF with the tail $\psi(t) \propto 1/t^{1+\mu}$ we use the method proposed by Kleinhans and Friedrich [118]. Results for the mobile mass and the first and second moments are shown in Fig. 14.

[1] A. Einstein, Über die von der molekularkinetischen Theorie der Wärme geforderte Bewegung von in ruhenden Flüssigkeiten suspendierten Teilchen, Ann. Phys. (Leipzig) **322**, 549 (1905).

[2] M. von Smoluchowski, Zur kinetischen theorie der Brownschen molekularbewegung und der suspensionen, Ann. Phys. (Leipzig) **326**, 756 (1906).

[3] W. Sutherland, A dynamical theory of diffusion for non-electrolytes and the molecular mass of albumin, Philos. Mag. **9**, 781 (1905).

[4] P. Langevin, Sur la theórie du mouvement brownien, C. R. Acad. Sci. **146**, 530 (1908).

[5] A. Fick, Über Diffusion, Ann. Phys. (Leipzig) **170**, 59 (1855).

[6] L. D. Landau and E. M. Lifshitz, *Physical Kinetics* (Butterworth Heinemann, Oxford, 1999).

[7] N. G. van Kampen, *Stochastic Processes in Physics and Chemistry* (North-Holland, Amsterdam, 1981).

[8] P. Lévy, *Processus stochastiques et mouvement brownien* (Stochastic processes and Brownian motion) (Gauthiers-Villars, Paris, 1948).

[9] B. D. Hughes, *Random Walks and Random Environments* (Oxford University Press, Oxford, 1995), Vol. 1.

[10] L. F. Richardson, Atmospheric diffusion shown on a distance-neighbour graph, Proc. R. Soc. London Ser. A **110**, 709 (1926).

[11] G. K. Batchelor, Diffusion in a field of homogeneous turbulence. II. Relative motion of particles, Math. Proc. Cambridge **48**, 345 (1952).

[12] J. Klafter, M. F. Shlesinger, and G. Zumofen, Beyond Brownian motion, Phys. Today **49**(2), 33 (1996).

[13] J.-P. Bouchaud and A. Georges, Anomalous diffusion in disordered media: Statistical mechanisms, models and physical applications, Phys. Rep. **195**, 127 (1990).

[14] R. Metzler and J. Klafter, The random walk's guide to anomalous diffusion: A fractional dynamics approach, Phys. Rep. **339**, 1 (2000).

[15] I. M. Sokolov, Models of anomalous diffusion in crowded environments, Soft Matter **8**, 9043 (2012).

[16] E. Barkai, Y. Garini, and R. Metzler, Strange kinetics of single molecules in living cells, Phys. Today **65**(8), 29 (2012).

[17] F. Höfling and T. Franosch, Anomalous transport in the crowded world of biological cells, Rep. Prog. Phys. **76**, 046602 (2013).

[18] D. Krapf and R. Metzler, Strange interfacial molecular dynamics, Phys. Today **72**(9), 48 (2019).

[19] K. Nørregaard, R. Metzler, C. Ritter, K. Berg-Sørensen, and L. Oddershede, Manipulation and motion of organelles and single molecules in living cells, Chem. Rev. **117**, 4342 (2017).

[20] E. E. Adams and L. W. Gelhar, Field study of dispersion in a heterogeneous aquifer: 2. Spatial moments analysis, Water Resour. Res. **28**, 3293 (1992).

[21] J. Drummond, N. Schmadel, C. Kelleher, A. Packman, and A. Ward, Improving predictions of fine particle immobilization in streams, Geophys. Res. Lett. **46**, 13853 (2019).

[22] N. Goeppert, N. Goldscheider, and B. Berkowitz, Experimental and modeling evidence of kilometer-scale anomalous tracer transport in an alpine karst aquifer, Water Res. **178**, 115755 (2020).

[23] K. Singha and S. M. Gorelick, Saline tracer visualized with three-dimensional electrical resistivity tomography: Field-scale spatial moment analysis, Water Resour. Res. **41**, W05023 (2005).

[24] R. Haggerty, S. M. Wondzell, and M. A. Johnson, Power-law residence time distribution in the hyporheic zone of a 2nd-order mountain stream, Geophys. Res. Lett. **29**, 18 (2002).

[25] A. F. Aubeneau, B. Hanrahan, D. Bolster, and J. L. Tank, Substrate size and heterogeneity control anomalous transport in small streams, Geophys. Res. Lett. **41**, 8335 (2014).

[26] K. H. Coats and B. D. Smith, Dead-end pore volume and dispersion in porous media, Soc. Petrol. Eng. J. **4**, 73 (1964).

[27] P. Gouze, Y. Melean, T. Le Borgne, M. Dentz, and J. Carrera, Non-Fickian dispersion in porous media explained by heterogeneous microscale matrix diffusion, Water Resour. Res. **44**, W11416 (2008).

[28] G. Margolin, M. Dentz, and B. Berkowitz, Continuous time random walk and multirate mass transfer modeling of sorption, Chem. Phys. **295**, 71 (2003).

[29] M. Dentz and B. Berkowitz, Transport behavior of a passive solute in continuous time random walks and multirate mass transfer, Water Resour. Res. **39**, 1111 (2003).

[30] B. Berkowitz, J. Klafter, R. Metzler, and H. Scher, Physical pictures of transport in heterogeneous media: Advection-dispersion, random-walk, and fractional derivative formulations, Water Resour. Res. **38**, 1191 (2002).

[31] Y. Edery, A. Guadagnini, H. Scher, and B. Berkowitz, Origins of anomalous transport in heterogeneous media: Structural and dynamic controls, Water Resour. Res. **50**, 1490 (2014).

[32] H. Krüsemann, A. Godec, and R. Metzler, First-passage statistics for aging diffusion in systems with annealed and quenched disorder, Phys. Rev. E **89**, 040101(R) (2014).

[33] J. Klafter and I. M. Sokolov, *First Steps in Random Walks* (Cambridge University Press, Cambridge, 2011).

[34] R. Metzler, J.-H. Jeon, A. G. Cherstvy, and E. Barkai, Anomalous diffusion models and their properties: Non-stationarity, non-ergodicity, and ageing at the centenary of single particle tracking, Phys. Chem. Chem. Phys. **16**, 24128 (2014).

[35] H. Scher and E. W. Montroll, Anomalous transit-time dispersion in amorphous solids, Phys. Rev. B **12**, 2455 (1975).

[36] C. Monthus and J.-P. Bouchaud, Models of traps and glass phenomenology, J. Phys. A: Math. Gen. **29**, 3847 (1996).

[37] E. Barkai and S. Burov, Packets of Diffusing Particles Exhibit Universal Exponential Tails, Phys. Rev. Lett. **124**, 060603 (2020).

[38] S. Mora and Y. Pomeau, Brownian diffusion in a dilute field of traps is Fickean but non-Gaussian, Phys. Rev. E **98**, 040101(R) (2018).

[39] W. Wang and E. Barkai, Fractional Advection-Diffusion-Asymmetry Equation, Phys. Rev. Lett. **125**, 240606 (2020).

[40] J. W. Kirchner, X. Feng, and C. Neal, Fractal stream chemistry and its implications for contaminant transport in catchments, Nature (London) **403**, 524 (2000).

[41] H. Scher, G. Margolin, R. Metzler, J. Klafter, and B. Berkowitz, The dynamical foundation of fractal stream chemistry: The origin of extremely long retention times, Geophys. Res. Lett. **29**, 1061 (2002).

[42] J. Klafter, A. Blumen, and M. F. Shlesinger, Stochastic pathway to anomalous diffusion, Phys. Rev. A **35**, 3081 (1987).

[43] J. M. Boggs, S. C. Young, L. M. Beard, L. W. Gelhar, K. R. Rehfeldt, and E. E. Adams, Field study of dispersion

in a heterogeneous aquifer: 1. Overview and site description, Water Resour. Res. **28**, 3281 (1992).

[44] C. Harvey and S. M. Gorelick, Rate-limited mass transfer or macrodispersion: Which dominates plume evolution at the Macrodispersion Experiment (MADE) site? Water Resour. Res. **36**, 637 (2000).

[45] R. Schumer, D. A. Benson, M. M. Meerschaert, and B. Baeumer, Fractal mobile-immobile solute transport, Water Resour. Res. **39**, 1296 (2003).

[46] Y. Zhang, D. A. Benson, and B. Baeumer, Moment analysis for spatiotemporal fractional dispersion, Water Resour. Res. **44**, W04424 (2008).

[47] G. Gao, H. Zhan, S. Feng, B. Fu, Y. Ma, and G. Huang, A new mobile-immobile model for reactive solute transport with scale-dependent dispersion, Water Resour. Res. **46**, W08533 (2010).

[48] M. T. van Genuchten and P. J. Wierenga, Mass transfer studies in sorbing porous media I. Analytical solutions, Soil Sci. Soc. Am. J. **40**, 473 (1976).

[49] R. Haggerty and S. M. Gorelick, Multiple-rate mass transfer for modeling diffusion and surface reactions in media with pore-scale heterogeneity, Water Resour. Res. **31**, 2383 (1995).

[50] J. D. Drummond, L. G. Larsen, R. González-Pinzón, A. I. Packman, and J. W. Harvey, Fine particle retention within stream storage areas at base flow and in response to a storm event, Water Resour. Res. **53**, 5690 (2017).

[51] J. A. Cunningham, C. J. Werth, M. Reinhard, and P. V. Roberts, Effects of grain-scale mass transfer on the transport of volatile organics through sediments: 1. Model development, Water Resour. Res. **33**, 2713 (1997).

[52] K. R. Roche, J. D. Drummond, F. Boano, A. I. Packman, T. J. Battin, and W. R. Hunter, Benthic biofilm controls on fine particle dynamics in streams, Water Resour. Res. **53**, 222 (2017).

[53] K. R. Roche, A. J. Shogren, A. Aubeneau, J. L. Tank, and D. Bolster, Modeling benthic versus hyporheic nutrient uptake in unshaded streams with varying substrates, J. Geophys. Res.: Biogeosc. **124**, 367 (2019).

[54] A. F. Aubeneau, B. Hanrahan, D. Bolster, and J. Tank, Biofilm growth in gravel bed streams controls solute residence time distributions, J. Geophys. Res.: Biogeosc. **121**, 1840 (2016).

[55] J. H. Writer, J. N. Ryan, S. H. Keefe, and L. B. Barber, Fate of 4-nonylphenol and 17β-estradiol in the Redwood River of Minnesota, Environ. Sci. Technol. **46**, 860 (2012).

[56] J. Drummond, A. Wright-Stow, P. Franklin, J. Quinn, and A. Packman, Fine particle transport dynamics in response to wood additions in a small agricultural stream, Hydrol. Process. **34**, 4128 (2020).

[57] J. D. Drummond, H. A. Nel, A. I. Packman, and S. Krause, Significance of hyporheic exchange for predicting microplastic fate in rivers, Environ. Sci. Technol. Lett. **7**, 727 (2020).

[58] J. L. Schaper, M. Posselt, J. L. McCallum, E. W. Banks, A. Hoehne, K. Meinikmann, M. A. Shanafield, O. Batelaan, and J. Lewandowski, Hyporheic exchange controls fate of trace organic compounds in an urban stream, Environ. Sci. Technol. **52**, 12285 (2018).

[59] B. M. Flier, M. C. Baier, J. Huber, K. Müllen, S. Mecking, A. Zumbusch, and D. Wöll, Heterogeneous diffusion in thin polymer films as observed by high-temperature single-molecule fluorescence microscopy, J. Am. Chem. Soc. **134**, 480 (2012).

[60] J. L. Keddie, R. A. Jones, and R. A. Cory, Size-dependent depression of the glass transition temperature in polymer films, Europhys. Lett. **27**, 59 (1994).

[61] Z. Yang, Y. Fujii, F. K. Lee, C. H. Lam, and O. K. Tsui, Glass transition dynamics and surface layer mobility in unentangled polystyrene films, Science **328**, 1676 (2010).

[62] Y. Liao, S. K. Yang, K. Koh, A. J. Matzger, and J. S. Biteen, Heterogeneous single-molecule diffusion in one-, two-, and three-dimensional microporous coordination polymers: Directional, trapped, and immobile guests, Nano Lett. **12**, 3080 (2012).

[63] A. V. Weigel, M. M. Tamkun, and D. Krapf, Quantifying the dynamic interactions between a clathrin-coated pit and cargo molecules, Proc. Natl. Acad. Sci. USA **110**, E4591 (2013).

[64] I. M. Sokolov, M. G. W. Schmidt, and F. Sagués, Reaction-subdiffusion equations, Phys. Rev. E **73**, 031102 (2006).

[65] A. A. Kurilovich, V. N. Mantsevich, K. J. Stevenson, A. V. Chechkin, and V. V. Palyulin, Complex diffusion-based kinetics of photoluminescence in semiconductor nanoplatelets, Phys. Chem. Chem. Phys. **22**, 24686 (2020).

[66] D. A. Benson and M. M. Meerschaert, A simple and efficient random walk solution of multi-rate mobile-immobile mass transport equations, Adv. Water Resour. **32**, 532 (2009).

[67] R. Haggerty, S. A. McKenna, and L. C. Meigs, On the late-time behavior of tracer test breakthrough curves, Water Resour. Res. **36**, 3467 (2000).

[68] R. Haggerty and S. M. Gorelick, Modeling mass transfer processes in soil columns with pore-scale heterogeneity, Soil Sci. Soc. Am. J. **62**, 62 (1998).

[69] B. Berkowitz, A. Cortis, M. Dentz, and H. Scher, Modeling non-Fickian transport in geological formations as a continuous time random walk, Rev. Geophys. **44**, RG2003 (2006).

[70] F. W. Schmidlin, Theory of trap-controlled transient photoconduction, Phys. Rev. B **16**, 2362 (1977).

[71] T. Sandev, A. V. Chechkin, N. Korabel, H. Kantz, I. M. Sokolov, and R. Metzler, Distributed-order diffusion equations and multifractality: Models and solutions, Phys. Rev. E **92**, 042117 (2015).

[72] B. Maryshev, M. Joelson, D. Lyubimov, T. Lyubimova, and M. C. Néel, Non Fickian flux for advection-dispersion with immobile periods, J. Phys. A: Math. Theor. **42**, 115001 (2009).

[73] T. R. Ginn, L. G. Schreyer, and K. Zamani, Phase exposure-dependent exchange, Water Resour. Res. **53**, 619 (2017).

[74] T. R. Ginn, Generalization of the multirate basis for time convolution to unequal forward and reverse rates and connection to reactions with memory, Water Resour. Res. **45**, W12419 (2009).

[75] J. H. Schulz, E. Barkai, and R. Metzler, Aging Effects and Population Splitting in Single-Particle Trajectory Averages, Phys. Rev. Lett. **110**, 020602 (2013).

[76] J. H. P. Schulz, E. Barkai, and R. Metzler, Aging Renewal Theory and Application to Random Walks, Phys. Rev. X **4**, 011028 (2014).

[77] H. Krüsemann, A. Godec, and R. Metzler, Ageing first passage time density in continuous time random walks and quenched energy landscapes, J. Phys. A: Math. Theor. **48**, 285001 (2015).

[78] D. N. Bradley, G. E. Tucker, and D. A. Benson, Fractional dispersion in a sand bed river, J. Geophys. Res. Earth Surf. **115**, F00A09 (2010).

[79] A. M. Michalak and P. K. Kitanidis, Macroscopic behavior and random-walk particle tracking of kinetically sorbing solutes, Water Resour. Res. **36**, 2133 (2000).
[80] W. Feller, *An Introduction to Probability Theory and its Applications* (Wiley, New York, 1971), Vol. 2.
[81] A. V. Chechkin, I. M. Zaid, M. A. Lomholt, I. M. Sokolov, and R. Metzler, Bulk-mediated surface diffusion along a cylinder: Propagators and crossovers, Phys. Rev. E **79**, 040105(R) (2009).
[82] R. Hilfer and L. Anton, Fractional master equations and fractal time random walks, Phys. Rev. E **51**, 848(R) (1995).
[83] T. Sandev, R. Metzler, and A. Chechkin, From continuous time random walks to the generalized diffusion equation, Frac. Calc. Appl. Anal. **21**, 10 (2018).
[84] R. Gorenflo, A. A. Kilbas, F. Mainardi, and S. V. Rogosin, *Mittag-Leffler Functions, Related Topics and Applications* (Springer, Berlin, 2014), Vol. 2.
[85] B. V. Gnedenko and A. N. Kolmogorov, *Limit Distributions for Sums of Random Variables* (Addison-Wesley, Reading, 1954).
[86] F. R. de Hoog, J. H. Knight, and A. N. Stokes, An improved method for numerical inversion of Laplace transforms, SIAM. J. Sci. Stat. Comput. **3**, 357 (1982).
[87] F. Johansson *et al.*, mpmath: A Python library for arbitrary-precision floating-point arithmetic, version 1.1.0 (2013), http://mpmath.org/
[88] I. Podlubny, *Fractional Differential Equations* (Academic Press, New York, 1998).
[89] A. V. Chechkin, R. Gorenflo, and I. M. Sokolov, Retarding subdiffusion and accelerating superdiffusion governed by distributed-order fractional diffusion equations, Phys. Rev. E **66**, 046129 (2002).
[90] T. R. Prabhakar, A singular integral equation with a generalized Mittag-Leffler function in the kernel. Yokohama Math. J. **19**, 7 (1971).
[91] H. J. Haubold, A. M. Mathai, and R. K. Saxena, Mittag-Leffler functions and their applications, J. Appl. Math. **2011**, 298629 (2011).
[92] N. Goldscheider, Fold structure and underground drainage pattern in the alpine karst system Hochifen-Gottesacker, Eclogae Geol. Helv. **98**, 1 (2005).
[93] O. Grisel *et al.*, scikit-learn/scikit-learn: scikit-learn 0.24.2, version 0.24.2, http://doi.org/10.5281/zenodo.4725836
[94] M. A. Thompson, J. M. Casolari, M. Badieirostami, P. O. Brown, and W. E. Moerner, Three-dimensional tracking of single mRNA particles in *Saccharomyces cerevisiae* using a double-helix point spread function, Proc. Natl. Acad. Sci. USA **107**, 17864 (2010).
[95] A. G. Cherstvy, O. Günther, C. Beta, and R. Metzler, Non-Gaussianity, population heterogeneity, and transient superdiffusion in the spreading dynamics of amoeboid cells, Phys. Chem. Chem. Phys. **20**, 23034 (2018).
[96] H. Murakoshi, R. Iino, T. Kobayashi, T. Fujiwara, C. Ohshima, A. Yoshimura, and A. Kusumi, Single-molecule imaging analysis of Ras activation in living cells, Proc. Natl. Acad. Sci. USA **101**, 7317 (2004).
[97] S. Manley, J. M. Gillette, G. H. Patterson, H. Shroff, H. F. Hess, E. Betzig, and J. Lippincott-Schwartz, High-density mapping of single-molecule trajectories with photoactivated localization microscopy, Nat. Methods **5**, 155 (2008).
[98] T. Kues, R. Peters, and U. Kubitscheck, Visualization and tracking of single protein molecules in the cell nucleus, Biophys. J. **80**, 2954 (2001).
[99] A. D. Fernández, P. Charchar, A. G. Cherstvy, R. Metzler, and M. W. Finnis, The diffusion of doxorubicin drug molecules in silica nanoslits is non-Gaussian, intermittent and anticorrelated, Phys. Chem. Chem. Phys. **22**, 27955 (2020).
[100] J.-H. Jeon, V. Tejedor, S. Burov, E. Barkai, C. Selhuber-Unkel, K. Berg-Sørensen, L. Oddershede, and R. Metzler, *In Vivo* Anomalous Diffusion and Weak Ergodicity Breaking of Lipid Granules, Phys. Rev. Lett. **106**, 048103 (2011).
[101] A. G. Cherstvy and R. Metzler, Population splitting, trapping, and non-ergodicity in heterogeneous diffusion processes, Phys. Chem. Chem. Phys. **15**, 20220 (2013).
[102] D. S. Grebenkov, Time-averaged mean square displacement for switching diffusion, Phys. Rev. E **99**, 032133 (2019).
[103] N. Tyagi and B. J. Cherayil, Non-Gaussian Brownian diffusion in dynamically disordered thermal environments, J. Phys. Chem. B **121**, 7204 (2017).
[104] F. Baldovin, E. Orlandini, and F. Seno, Polymerization induces non-Gaussian diffusion, Front. Phys. **7**, 124 (2019).
[105] A. Sabri, X. Xu, D. Krapf, and M. Weiss, Elucidating the Origin of Heterogeneous Anomalous Diffusion in the Cytoplasm of Mammalian Cells, Phys. Rev. Lett. **125**, 058101 (2020).
[106] E. Yamamoto, T. Akimoto, A. Mitsutake, and R. Metzler, Universal Relation between Instantaneous Diffusivity and Radius of Gyration of Proteins in Aqueous Solution, Phys. Rev. Lett. **126**, 128101 (2021).
[107] M. Hidalgo-Soria and E. Barkai, Hitchhiker model for Laplace diffusion processes, Phys. Rev. E **102**, 012109 (2020).
[108] A. V. Weigel, B. Simon, M. M. Tamkun, and D. Krapf, Ergodic and nonergodic processes coexist in the plasma membrane as observed by single-molecule tracking, Proc. Natl. Acad. Sci. USA **108**, 6438 (2011).
[109] C. Manzo, J. A. Torreno-Pina, P. Massignan, G. J. Lapeyre, Jr., M. Lewenstein, and M. F. Garcia Parajo, Weak Ergodicity Breaking of Receptor Motion in Living Cells Stemming from Random Diffusivity, Phys. Rev. X **5**, 011021 (2015).
[110] J.-H. Jeon, M. Javanainen, H. Martinez-Seara, R. Metzler, and I. Vattulainen, Protein Crowding in Lipid Bilayers Gives Rise to Non-Gaussian Anomalous Lateral Diffusion of Phospholipids and Proteins, Phys. Rev. X **6**, 021006 (2016).
[111] C. E. Wagner, B. S. Turner, M. Rubinstein, G. H. McKinley, and K. Ribbeck, A rheological study of the association and dynamics of MUC5AC gels, Biomacromol. **18**, 3654 (2017).
[112] A. G. Cherstvy, S. Thapa, C. E. Wagner, and R. Metzler, Non-Gaussian, non-ergodic, and non-Fickian diffusion of tracers in mucin hydrogels, Soft Matter **15**, 2526 (2019).
[113] W. He, H. Song, Y. Su, L. Geng, B. J. Ackerson, H. B. Peng, and P. Tong, Dynamic heterogeneity and non-Gaussian statistics for acetylcholine receptors on live cell membrane, Nat. Commun. **7**, 11701 (2016).
[114] G. J. Schütz, H. Schindler, and T. Schmidt, Single-molecule microscopy on model membranes reveals anomalous diffusion, Biophys. J. **73**, 10730 (1997) .
[115] P. H. Lommerse, B. E. Snaar-Jagalska, H. P. Spaink, and T. Schmidt, Single-molecule diffusion measurements of H-Ras at the plasma membrane of live cells reveal

microdomain localization upon activation, J. Cell Sci. **118**, 1799 (2005).

[116] T. Sungkaworn, M. L. Jobin, K. Burnecki, A. Weron, M. J. Lohse, and D. Calebiro, Single-molecule imaging reveals receptor-G protein interactions at cell surface hot spots, Nature (London) **550**, 543 (2017).

[117] A. M. Alexander and S. D. Lawley, Reaction-subdiffusion equations with species-dependent movement, SIAM J. Appl. Math. **81**, 2457 (2021).

[118] D. Kleinhans and R. Friedrich, Continuous-time random walks: Simulation of continuous trajectories, Phys. Rev. E **76**, 061102 (2007).